Biosensing of Bacterial Secretions via Topological Defects at Smectic Interfaces

*Vajra S. Badha,[a] Tagbo H.R. Niepa,[b,c] and Mohamed Amine Gharbi[a]**

[a] Department of Physics, University of Massachusetts Boston, Boston, MA 02125, USA

[b] Department of Chemical Engineering, Carnegie Mellon University, Pittsburgh, PA 15213, USA

[c] Department of Biomedical Engineering, Carnegie Mellon University, Pittsburgh, PA 15213, USA

Keywords: Biosensing, smectic liquid crystal interface, bacteria, topological defects, liquid crystal anchoring

Abstract

Characterizing the anchoring properties of smectic liquid crystals (LCs) in contact with bacterial solutions is crucial for developing biosensing platforms. In this study, we investigate the anchoring properties of a smectic LC when exposed to *Bacillus subtilis* and *Escherichia coli* bacterial suspensions using interfaces with known anchoring properties. By monitoring the

optical response of the smectic film, we successfully distinguish different types of bacteria, leveraging the distinct changes in the LC's response. Through a comprehensive analysis of the interactions between bacterial proteins and the smectic interface, we elucidate the potential underlying mechanisms responsible for these optical changes. Additionally, we introduce the utilization of topological defects; the focal conic domains (FCDs), at the smectic interface as an indicative measure of the bacterial concentration. Our findings contribute to the understanding of bacteria-LC interactions and demonstrate the significant potential of smectic LCs and their defects for biosensing applications, paving the way for advancements in pathogen detection and protein-based sensing.

Introduction

Biosensors are critical tools in detecting bacteria,[1,2] viruses,[3,4] and other molecules[5] which are responsible for various infections and environmental impacts. Their application is essential in healthcare for identifying bacterial presence and monitoring infections,[6] as well as in food safety [7,8] and environmental monitoring. Traditional methods for bacterial detection include techniques like plate culturing,[9] Polymerase Chain Reaction (PCR),[10,11] and Enzyme-Linked Immunosorbent Assay (ELISA).[12] While accurate and reliable, these methods are often time-consuming and require skilled technicians. To address these limitations, research has increasingly focused on developing alternative biosensing techniques that are faster, simpler, and more accessible to non-experts. Among these, liquid crystal (LC) biosensors have shown particular promise for their high sensitivity and ability to produce rapid optical signals in response to bacterial presence.[13]

LCs are a versatile class of materials with properties between those of liquids and solids. They can flow like fluids while maintaining some molecular orientations like crystals.[14] LCs are usually made of elongated molecules that can align along particular directions. Depending on these directions and the arrangement of molecules, one can distinguish different phases of LCs. Some examples include the nematic phase, in which molecules are oriented along a common direction, known as the director; the cholesteric phase, where molecules are assembled into helical structures; and the smectic phase, in which molecules form layered structures. These different arrangements give the LCs unique optical properties making them useful in a variety of applications ranging from LC displays (LCDs)[15,16] and smart windows[17] to optical filters[18] and thermometers.[19]

LCs are also valuable for biosensing applications due to their ability to rapidly respond to changes in their environments with very high sensitivity. When an LC is in contact with a biological material, it can adjust its optical properties by changing its color or brightness due to its birefringence. This transformation can be exploited to detect the existence of analytes and measure their concentrations. An advantage of using LCs in biosensing is that they can be easily tailored to interact with specific target molecules to increase their specificity. Additionally, they are relatively simple and inexpensive to fabricate. For this reason, they were used in a wide range of applications, including in the detection of pH,[20] glucose,[21] enzymatic activity,[22] chemical[23–25] and other biochemical compounds.[26] Other applications include environmental monitoring,[27,28] food safety,[29] medical diagnostics,[30] drug discovery,[31] and pathogen detection.[32]

The common molecular orientation of LCs can be realigned parallel or perpendicular to the surface in contact.[33] This property is called anchoring and is very well studied for various LC phases.[34,35] A uniform or degenerate planar alignment is usually obtained when the LC molecules align parallel

to the surfaces confining the LC film whereas, a homeotropic alignment is achieved when the LC molecules align perpendicular to the surfaces. However, it is also possible to create a hybrid texture when the LC anchoring at the confining surfaces is different; for example, planar on one side and perpendicular on the other one.[36]

Depending on the phase of the liquid crystal (LC), various topological defects may form, each with a distinct optical response when viewed through crossed polarizers. By leveraging these optical responses, previous studies have established the foundational principles of advanced LC biosensor technology.[37–41] These sensors operate by inducing an orientational reorganization of LC molecules, producing an optical response detectable via imaging techniques. This principle was demonstrated by Popov *et al.* [42] and Pani *et al.*,[43] confirming the effectiveness of LCs as sensing systems.

Although many studies show the ability of LC-based systems to sense multiple analytes with specificity, as mentioned so far, most of these studies focused on nematic,[44,45] cholesteric,[46,47] and blue phase LCs,[48] as the element for sensing. Additionally, these systems only exploited the optical birefringence of the LC[49] as an output to be transduced. Little is known about the potential of other LC phases and their topological defects in biosensing applications, such as smectic LCs, despite the previous literature supporting the fact that these materials are much more sensitive to analytes than other LC phases.[35,50] This is attributed to the defects in smectic LCs—specifically, focal conic domains (FCDs)—which serve as the mechanism for detecting changes in anchoring properties at the interface. These defects are highly stable, especially compared to other types of defects in other LC phases, and are uniquely characteristic of the smectic phase under hybrid anchoring conditions.

In this work, we explore smectic LCs and their defects known as FCDs. We investigate their sensing potential and demonstrate their ability to detect the presence of living microorganisms. A focal conic domain contains smectic layers wrapped around two defect lines that have the shape of an ellipse and a parabola. The two lines are in two planes perpendicular to each other and pass through each other's focal point. FCDs are formed extending through the bulk of the LC on cooling from the isotropic or nematic phase to the smectic-A phase. They can also be forced as a thicker film by sandwiching the LC between two surfaces with opposite anchoring conditions, that is, a planar (parallel) anchoring condition at one interface of the LC film and a homeotropic (perpendicular) anchoring condition at the second interface. These opposing boundary conditions can be satisfied by the LC only when the LC smectic layers are bent to conform to both the interfaces, forming the focal conic domains. The two defect lines of each focal conic domain adopt in these films the shape of a straight line and a circle i.e., the layers form a system of nested tori. We illustrate how these defects, the focal conic domains (FCDs), can distinguish between various cells and also approximate their concentrations. We also discuss the interaction of living microorganisms with the smectic interface and explain how this system can be exploited in biosensing applications to detect pathogens.

Materials and Methods

Preparation of the smectic film

Our experimental system studies the interaction between two types of living microorganisms, *Bacillus subtilis* (*B. subtilis* 6051, ATCC) and *Escherichia coli* (*E. coli* 700926, ATCC), with a smectic film confined in cross shaped polydimethylsiloxane (PDMS) holes, measuring 300 μm

wide and 75 μm deep, under controlled anchoring conditions, as shown in **Figure 1-a**. The PDMS material was utilized because it is biologically inert,[51] non-toxic[52] and can be easily fabricated into microstructures. In all our experiments, we prepare the samples, add the analyte solution, and collect the imaging data within 15 minutes overall and 5 minutes from the time of adding the analyte solution. In this short period of time, we did not notice any change in either the properties of the PDMS or the structure of FCDs within the smectic film. (**see Supplementary Information for more details**)

The PDMS crosslinking solution was prepared by mixing the Silicone elastomer and crosslinking curing agent (Sylgard 184 Silicone Elastomer Kit, Dow) in the ratio of 10:1. The experimental cells were first fabricated using photolithography (Microlight 3D) by printing the negative of the required microstructures with the photoresist (AZ125nXT 10A, Micro chemicals) onto a silicon substrate. After completing the photolithography process, a crosslinking PDMS mold was poured onto these microstructures and baked at 70 °C for 90 minutes.

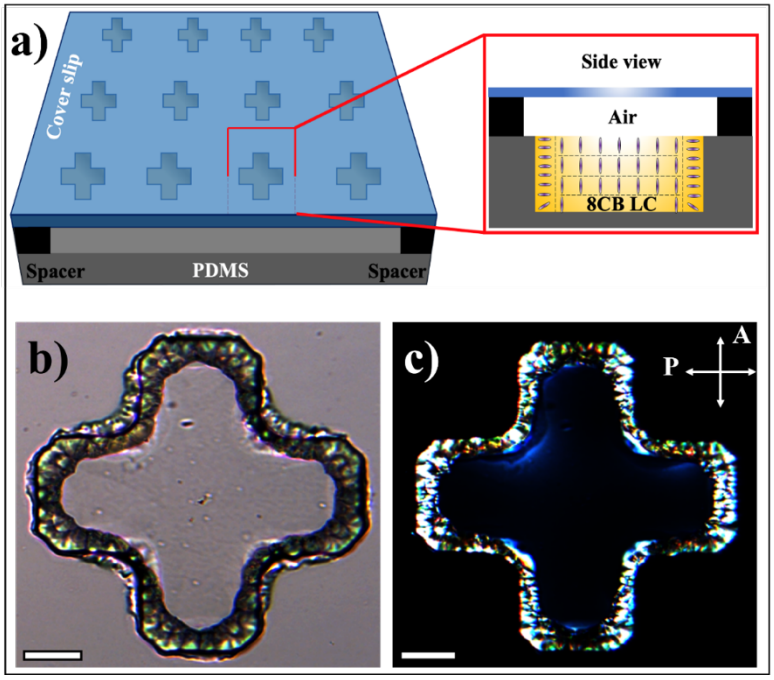

Figure 1. Creation of smectic films. (a) Experimental setup used to confine the smectic film into cross shaped holes made of PDMS. The side view shows the homeotropic alignment of the smectic molecules when confined between the PDMS and air. (b) Brightfield and (c) polarizing optical microscopy (POM) images of the smectic film between the PDMS and air. The scale bars are 50 μm.

The LC material utilized in this study is the 4-octyl-4′-cyanobiphenyl (8CB, Sigma Aldrich), which exhibits four phases depending on the temperature: a crystal phase below 21.35 °C, a smectic A phase between 21.35 °C and 33.35 °C, a nematic phase between 33.35 °C and 40.35 °C, and an isotropic phase above 40.35 °C.[53] We choose the 8CB because this material presents a smectic A phase at room temperature, in which the molecules are arranged in parallel layers but their director is perpendicular to the plane of these layers. Smectic LCs are characterized

by their high viscosity and strong molecular order, which makes them useful for many applications including biosensing.[54,55]Although the 8CB is toxic for living microorganisms, it does not come into direct contact with bacteria due to the interfacial hydrodynamic interactions that prevent the cells from penetrating into the 8CB.[56] The cells can survive at the smectic interface for more than 70 minutes, providing sufficient time for our analysis.

To prepare the experimental sample, the 8CB is added to the PDMS holes in its smectic phase using a spatula and subsequently by sweeping a glass cover slip over the holes to pack the LC. Further, the LC is heated to the isotropic phase using a heat gun to reduce viscosity and form a uniform layer before allowing it to cool down to room temperature. In our experiments, we tested different PDMS shapes with different sizes and chose to work with the cross shaped holes because they were found to help stabilize the smectic films in contact with the aqueous solutions instead of adding surfactants. Our goal here is to make sure that the optical response of the smectic interface is only due to its interaction with the bacterial solution and not due to other chemicals.

Confining living microorganisms at the smectic interface

The model microorganisms *B. subtilis* (6051, ATCC) and *E. coli* (700926, ATCC) were selected to represent a wide range of bacteria with different physical, physiological, and chemical properties. While the *E. coli* is Gram-negative and 1-2 μm long,[57] *B. subtilis* is gram-positive and measures 2-6 μm.[58] *E. coli* has a prominent outer membrane but *B. subtilis* cell lacks it.[59]

As a result, *B. subtilis* secretes proteins and other cellular molecules directly into its surrounding environment.

Terrific Broth (TB) (Sigma Aldrich) was used to grow the overnight cultures (12-14 hours) of *B. subtilis* and *E. coli* at 33°C and 37°C in the incubator (MaxQ 4450, Thermo Scientific), respectively. Dry powder of the bacteria was added into ~10 mL TB in a sterile 25 mL conical flask and placed into a shaking incubator at appropriate temperatures and 80 rpm. The growth was confirmed by a manual optical observation of turbidity of the TB solution.

Once the smectic LC layer was established, deionized water, TB with, and without microorganisms were introduced on separate samples to study their effect on the smectic anchoring. 15 μl of the culture media without washing was added to the top of LC and covered with a glass coverslip after placing 25 μm spacers. Imaging was performed in transmission mode from the top using a Leica DM6M microscope and recorded with a Leica DMC5400 high resolution camera. Images were collected in brightfield and polarized optical microscopy (POM) and were transferred onto FIJI for further analysis. This allowed us to visualize the effects of introducing microorganisms on the LC anchoring and investigate if smectic can serve as potential biosensors for the detection of bacteria.

Protein identification in the bacterial solutions

To understand the interaction between the smectic interface and *E. coli* or *B. subtilis* cells, we used a Bruker tims-TOF HT mass spectrometer to identify the proteins in their solutions.

Overnight cultures of bacteria were centrifuged at ~ 3250 g for 10 minutes, and 1 mL of supernatant was separated for further preparation. The proteins were precipitated out from the supernatant by adding 4 ml of acetone to the 1 ml of the supernatant and centrifuged at 2300 g to separate the proteins. Next, the pellets were resuspended in a 1 mL Optima water and buffer exchanged using pre-rinsed Amicon 3 kDa MWCO filters into Optima water before centrifuging thrice at 16000 g. The eluants were brought to 200 µL, and Bicinchoninic acid (BCA) assay was performed to determine protein concentration (see **Supplementary Information Table S1**).

Preparation of bacterial solutions

To understand the effect of microorganism concentration on the topological defects formed in smectic, a series of *E. coli* concentrations were prepared by inoculating *E. coli* (ATCC 700926) and allowing it to grow over a period of 12 hours. To the overnight culture, we add sterile TB in the ratios of 1:9 (1 part of *E. coli* culture to 9 parts of sterile TB), 2:8, 4:6, 6:4, and 8:2 to dilute the bacterial concentration. The undiluted overnight culture was considered the highest concentration, and sterile TB was considered zero concentration.

Determination of bacterial concentration

Two methods were employed to determine the density of bacteria in the studied solutions. The first method involved measuring optical density at 600 nm (OD_{600}) using a

spectrophotometer (Cary 60 UV-Vis by Agilent Technologies). The second method utilized image processing analysis with FIJI to count the number of cells in the samples. We have observed that while OD_{600} values can provide some information to quantify bacterial cell counts, these values can vary significantly between different spectrophotometers and sample preparations. This variation is partly due to the fact that OD_{600} measurements include absorbance and scattering by extracellular products secreted by the cells, not just the cells themselves. Consequently, the OD_{600} technique becomes less reliable, even at values as low as 0.3.[60] To address these limitations, we used an image processing method. By obtaining images of the samples and counting the number of cells, this method allows us to estimate the instantaneous concentration of bacteria at the time of sample preparation.

Using FIJI, we counted the number of cells in a 50 μm x 50 μm x 25 μm volume region (**see Supplementary Information Figure S2**) and extrapolated this to a 1 mL volume for an approximate estimate of the bacterial cell concentration per mL. As the choice of the region influences the calculation of bacterial concentration, we minimized the error in our estimation by counting the number of bacteria at six distinct, randomly chosen locations in the sample to eliminate bias. We report the average of these six estimates as the average concentration of the bacterial solution (**see Supplementary Information Table S6 and Figure S3**). Compared to the average concentration, the standard deviation, standard error, and percentage error values were low (**see Supplementary Information Figure S3**). This is why we believe our protocol provides a more reliable estimation of bacterial concentration than OD_{600}.

Results and Discussion

Anchoring properties of the smectic film

To study how smectic 8CB reacts to different anchoring conditions, we conducted a reference analysis to observe its texture when confined between PDMS and air, PDMS and deionized water, and PDMS and TB. This analysis aimed to identify the various molecular alignments that the smectic can adopt before bacteria are added. To do this, we prepared the PDMS sample with 8CB, as described in the experimental section. Next, we added 25 μm spacers on top of the PDMS and covered the setup with a glass coverslip, as shown in **Figure 1-a**. **Figures 1-b and 1-c** display the corresponding brightfield and POM images of the smectic film in this configuration. These images revealed the presence of a dark region that persists while rotating the polarizers, confirming that the 8CB molecules are perpendicular to both surfaces, the PDMS[61] and air. [62]

When deionized water is used instead of air, as shown in **Figure 2-a**, a different texture is observed both in bright field and between crossed polarizers. The dark regions that indicate homeotropic alignment disappear and are replaced by bright areas decorated with smectic defects known as FCDs (**Figures 2-b** and **2-c**). These defects consist of layers wrapping around an ellipse and a hyperbola, which contain all singular points.[63–65] The size of these defects depends on the thickness of the LC film and the curvature at the boundaries.[66] The formation of FCDs suggests that the smectic film has a hybrid anchoring — planar on one surface and

perpendicular on the opposite surface. As the PDMS imposes a homeotropic alignment, therefore, the smectic has a planar anchoring in contact with water.

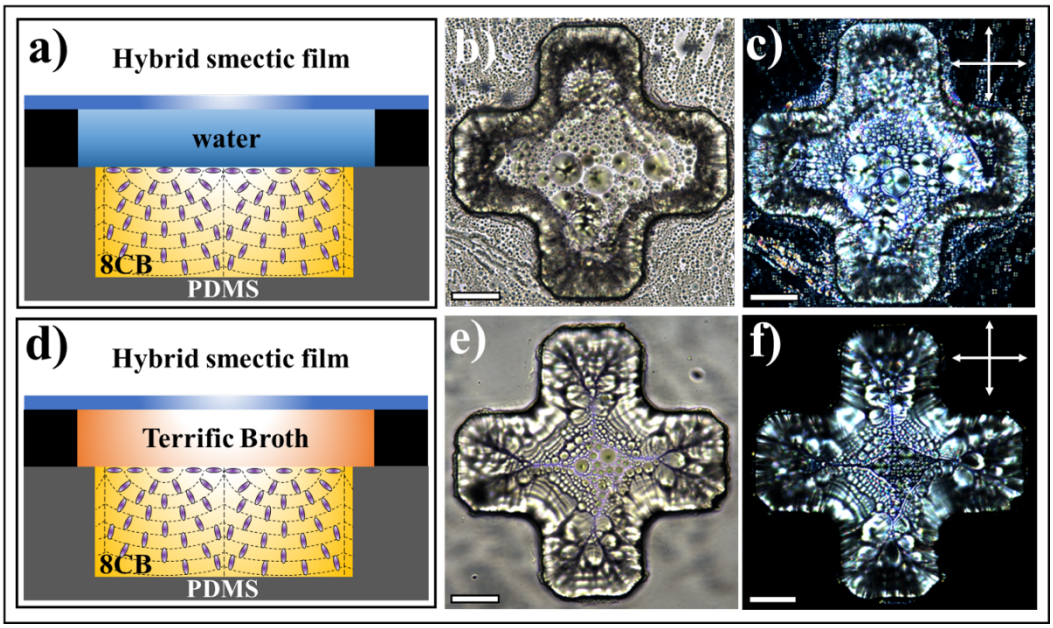

Figure 2. Texture of the 8CB in contact with water and TB. (a) Side view sketch of the LC confined between PDMS and water. Top view of the optical responses of the LC confined between PDMS and Water under brightfield (b), and POM (c). (d) Side view sketch of the LC confined between the PDMS and TB. Top view of the optical responses of the LC confined between the PDMS and TB under brightfield (e) and POM (f). The scale bars are 50 μm.

Next, we set up the smectic LC in contact with the TB instead of water, as shown in **Figure 2-d**. We chose to test the LC anchoring in contact with the TB because this fluid was used to grow *B. subtilis* and *E. coli* cells. The optical images demonstrate a flat and stable LC-TB interface decorated with FCDs, as presented in **Figures 2-e** and **2-f**. The formation of FCDs confirms that the anchoring of the 8CB is planar in contact with the TB, similar to that with

water. These results also indicate that the smectic interface is sensitive to the fluids it contacts. This information can be used to explore how the smectic behaves when in the presence of bacteria and their secreted metabolites.

Interaction of *B. subtilis* and *E. coli* cultures with a smectic interface

To understand how smectic LCs interact with living microorganisms, we first introduced a TB solution with *B. subtilis* cells on the top of the 8CB film, as depicted in **Figure 3-a**. Our results show that the smectic film forms a texture without any topological defects (see **Figure 3-b**), unlike pure TB, which has FCDs at the interface. Additionally, the smectic film remains dark when observed between crossed polarizers and rotated (see **Figure 3-c**). This suggests that the 8CB has a homeotropic alignment when in contact with the *B. subtilis* suspension in TB. Subsequently, when we repeat the experiment with *E. coli* cells instead of *B. subtilis* (see **Figure 3-d**), we observe a distinctly different response, as shown in **Figures 3-e** and **3-f**. The 8CB film forms defects; the FCDs, and the texture is similar to that achieved with deionized water and pure TB. This interaction process is both instantaneous and irreversible, indicating that once the alignment of the liquid crystal is affected by the bacterial secretions, it does not revert to its original state. This result indicates that the anchoring of the 8CB is planar when in contact with the *E. coli* suspension in the culture medium. While the initial aim of our study was to understand how smectic LCs interact with living microorganisms, it became

apparent that the observed changes were primarily due to the secreted proteins, rather than direct interactions with the bacterial cells themselves.

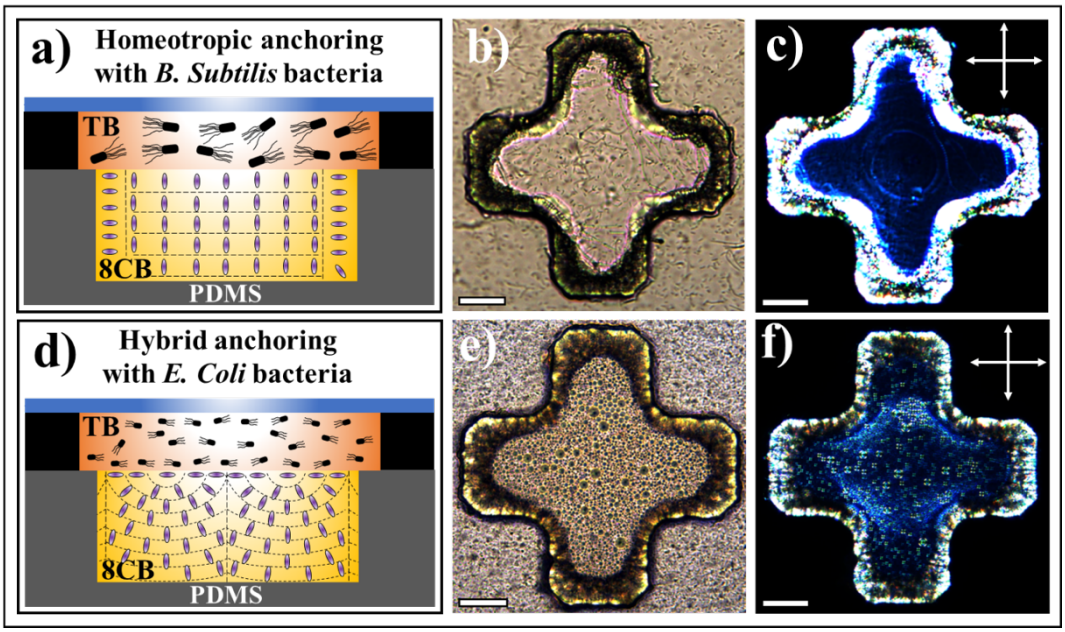

Figure 3. Interaction of the smectic interface with living microorganisms. (a) Side view sketch of the LC confined between PDMS and TB solution with B. subtilis cells. The Corresponding optical responses of the smectic LC under brightfield (b) and POM (c). These images indicate that the anchoring of the 8CB film is homeotropic. (d) Side view sketch of the LC confined between PDMS and TB with E. coli cells. The corresponding optical responses of the smectic LC under brightfield (e) and POM (f). These images indicate that the anchoring of the 8CB film is hybrid. The scale bars are 50 μm.

Based on the varying optical response of the LC film and the formation of defects, it is plausible to conclude that the smectic interface may sense the two microorganisms distinctly, and therefore, act as a biosensor. A LC biosensor operates on the principle that when specific

biomolecules interact with the interface, they cause changes in the LC film's molecular arrangement and optical properties, as shown in the work of Brake *et al.*[67] These changes can be detected and analyzed, providing information about the presence, concentration, or activity of the target biological substances such as insulin.[68] Therefore, it is crucial to understand how the smectic responds differently to *B. subtilis* and *E. coli* cells in order to exploit this property for biosensing.

These results suggest that it is the proteins secreted by the bacteria that are responsible for the observed optical responses in the LC film. As bacteria metabolize nutrients, they release a variety of proteins, including lipoproteins, into their environment. It is known that bacteria release a variety of proteins during their growth process, while metabolizing nutrients. Different types of bacteria secrete different proteins. For instance, previous studies have revealed that *B. subtilis* and *E. coli*, all strains combined, secrete at least 300[69] and 1600[70,71] proteins, respectively. This suggests that the difference in optical response with our system could be due to the variation between the cells and the secreted metabolites. Therefore, the distinct responses of the liquid crystal film to *B. subtilis* and *E. coli* can be attributed to the specific proteins secreted by each microorganism, rather than direct contact with the bacterial cells.

To prove this hypothesis, we conducted a proteomics study to determine what type of proteins *B. subtilis* and *E. coli* release during their growth in TB (see **Tables S1 and S2** in **Supplementary Information)**. Our data show that the *B. subtilis* cells releases approximately 77 proteins, whereas *E. coli* cells release 361 proteins. Interestingly, only 20 proteins were

found to be common between the two microorganisms (see **Table S3** in **Supplementary Information**). In total, *B. subtilis* released 57 unique proteins, while *E. coli* released 341. These findings highlight the significant variation in protein composition between the two types of bacteria.

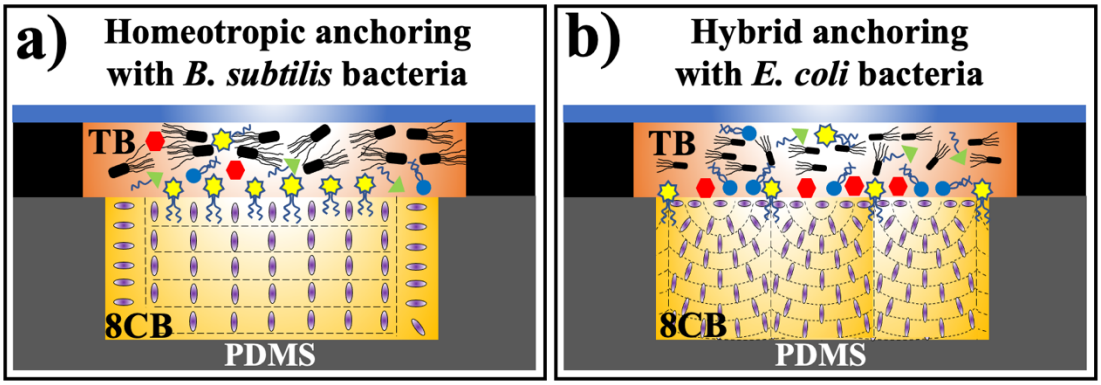

Figure. 4 Adsorption of proteins at the smectic interface. (a) Sketch showing how proteins in a *B. subtilis* solution integrate their hydrophobic tails into the LC causing a homeotropic alignment of the 8CB molecules at the interface. (b) Sketch showing how proteins in an *E.coli* solution accumulate at the smectic interface causing the FCDs to decrease in size. We note that the surfactant-like representation of proteins in these figures is a simplified illustration, intended to help visualize how such proteins may penetrate the smectic interface and influence anchoring.

Previous groups have shown that *B. subtilis* cells release highly hydrophobic compounds,[72,73] while *E. coli* cells produce them in small quantities. These molecules are usually lipoproteins that can adsorb at the interface between the LC and the TB. Due to the hydrophobic nature of

their hydrocarbon tails, the lipoproteins could integrate via their tails into the LC against the aqueous interface, causing a possible re-orientation of the LC molecules from planar to homeotropic.[38,74] This mechanism could explain the homeotropic alignment of the 8CB molecules in contact with the TB and *B. subtilis* cells, as shown in **Figure 4-a**. Our proteomic data show that *B. subtilis* cells produced only one type of lipoprotein, while *E. coli* produced seven (**see Tables S4 and S5 in Supplementary Information**). Since only *B. subtilis* cells induce homeotropic anchoring, it is plausible that the hydrophobic components secreted by *B. Subtilis* might induced stronger re-orientation of the LC compared to those secreted by *E. coli*, which corroborated previous studies.[72,73]

It is important to note that while the proteomics technique helped us identify the types of proteins secreted by both cells, it did not provide information about the specific elements responsible for switching the anchoring properties at the smectic interface nor their quantities. This limitation arises because proteomics offers only qualitative information about the biomolecules present in the bacterial suspensions. Therefore, further investigations are needed to characterize the exact elements.

Another significant result we noticed is that in the case of *E. coli* cells, the structure of FCDs at the smectic interface was different from one sample to another, particularly, their size changes (**Figure 2-e** and **Figure 3-e**). To better understand the origin of this variation, we investigated the sensitivity of the 8CB biosensing by exposing the LC to various dilution of *E. coli* at concentrations ranging from zero to 3.07 x 10^9 cells/mL. The images were analyzed using the oval tool in FIJI[75] **(see supplementary Figure S4)** to determine the average area of

the defects. Here, we neglect the defects that are less than 30 μm² because these defects are known to be unstable and generally are not affected by the concentration of bacteria. Optical images in **Figures 5-a to 5-f** show the formation of defects at all concentrations, but their size distribution varies as a function of *E. coli* density. These measurements indicate that the average size of FCDs linearly decreases from ~ 85 μm² to 40 μm² with the concentration of *E. coli* changing from ~ 0 cells/mL to 3.1 x 10^9 cells/mL (**Figure 5-g**). This clearly indicates that either the bacteria secretions or their dynamics are contributing to the change in FCDs' size.

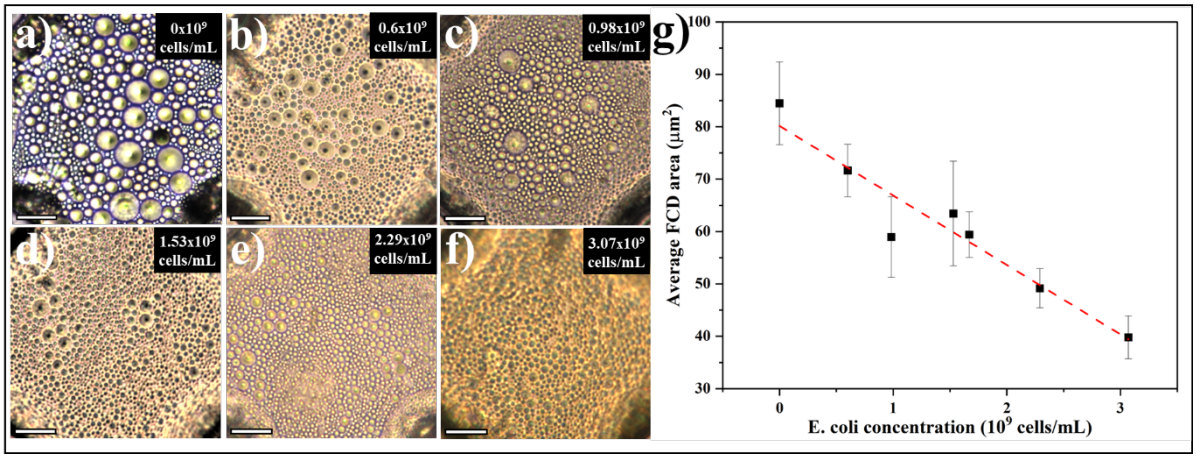

Figure 5. Effect of E. coli concentration on the size distribution of the FCD defects. (a-f) The size of the FCDs decreases with the concentration of E. coli. The scale bars are 25 μm. (g) Plot of the average FCD area as a function of E. coli concentration. The bars represent the standard error. The dashed line is a linear fit of the data with an R2 value of 0.85.

To clarify if the bacterial dynamics play a role in forming FCDs with different sizes, we repeated the same experiments with TB solutions containing only the secretions, prepared by removing the *E. coli* cells. A 10 mL overnight *E. coli* culture was pipetted into a 15 mL screw

cap centrifuge tube and centrifuged at ~ 3250 g for 10 minutes. The supernatant containing bacterial secretory proteins was separated from the pellet and diluted by adding fresh and sterile TB. The dilutions prepared were 1/2, 1/4, 1/8, 1/16, and 1/32 of the supernatant concentration. The results obtained in **Figures 6-a to 6-f** were similar to those obtained with the solutions containing live *E. coli* (**Figure 5)**. The FCDs' size decreases linearly with the concentration of the protein solution (**Figure 6-g**). Although the bacteria were absent, the TB solution containing only the proteins elicited a response similar to the TB solution containing the *E. coli* cell*s*. These results indicate that bacterial motility has no role in creating defects. The physical presence of bacteria has a negligible contribution, while bacterial secretions are responsible for the formation of FCDs and controlling their sizes. This further indicates that a higher concentration of the proteins may stabilize the FCDs while restricting their expansion to a smaller size. The concentration of the secreted proteins is then forcing the FCDs to assume a smaller size by wrapping the smectic layers tighter to form a more significant number of smaller defects, as shown in **Figure 4-b**.

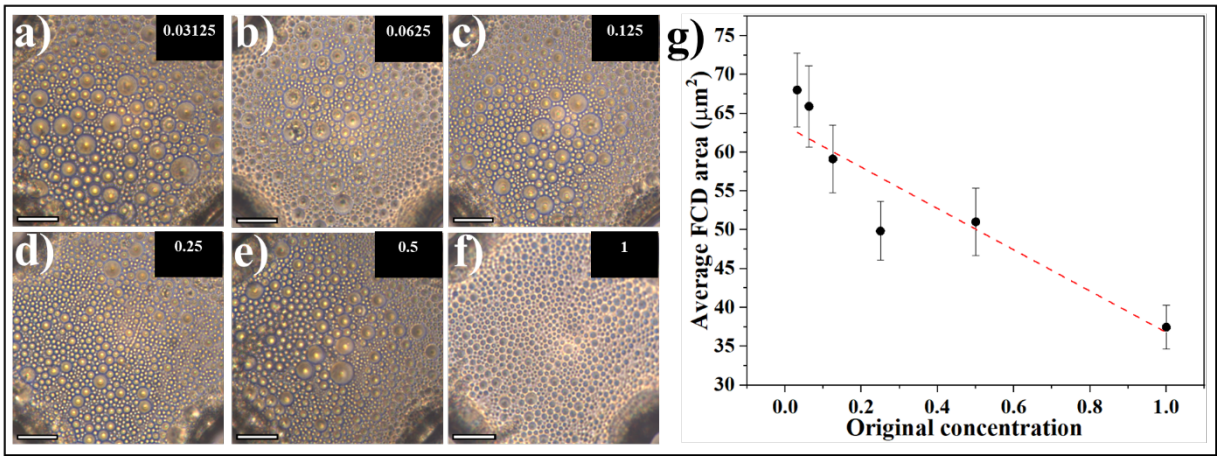

Figure 6. Effect of proteins released by E. coli cells on the size distribution of FCD defects. (a-f) The size of the FCDs decreases with the concentration of E. coli proteins. The scale bars are 25 μm. (g) Plot of the average FCD area as function of the E. coli protein solution concentration. The list of proteins present in the solution can be found in the Supplementary Information Table S1. The bars represent the standard error. The dashed line is a linear fit of the data with an R2 value of 0.86.

To confirm if these results apply to *B. subtilis*, we conducted similar experiments with *B. subtilis* secretions after removing the live cells. The results were consistent: the smectic anchoring switched from planar to homeotropic, confirming that the cells and their dynamics have a negligible effect on the properties of the smectic interface. All these results demonstrate the potential of our smectic LC system to distinguish different types of living microorganisms due to the vast difference in their secreted proteins. They also show how smectic defects can be employed to estimate the concentration of the released biomolecules. Still further investigations are needed to establish what type of secreted molecules contribute to the smectic behavior, distinguishing the sensing of *E. coli* vs. *B. subtilis*. This is part of our on-going work. Nonetheless, these findings open doors for various applications in biomedical diagnostics, environmental monitoring, and the development of improved biosensors.

Conclusion

In this study, we successfully characterized the anchoring properties of smectic LCs in contact with *B. subtilis* and *E. coli* bacterial solutions using interfaces with known properties. Through our experiments, we demonstrated the ability of the smectic LC interface to be sensitive to two different types of bacteria and elicit different responses. The outcome was achieved by observing the changes in the optical properties of the smectic film upon adding the bacterial solutions. Furthermore, we hypothesized the mechanism behind these changes by exploring the interactions between the proteins released by the bacteria and the smectic interfaces. Our findings also revealed the potential utility of topological defects at the smectic interface, specifically focal conic domains (FCDs), as a means to quantify the concentration of bacteria based on the amount/concentration of proteins present in the sample cultures.

These results highlight the promising potential of smectic LCs and their defects in biosensing applications. To expand this work, future research should aim to develop a deeper understanding of the biomolecules interacting with the smectic interface. "Future efforts should focus on optimizing the biosensor design, broadening the range of microorganisms studied, and enhancing specificity. Additionally, improving the biocompatibility of the biosensor by investigating non-toxic smectic liquid crystals or alternative materials with similar interfacial properties is essential. Expanding the biosensor's potential applications, particularly in biomedical diagnostics, environmental monitoring, and other fields requiring rapid and sensitive detection, also represents a promising direction for further research."

Corresponding Author

* Mohamed.Gharbi@umb.edu

Author contributions

V.S.B and M.A.G. designed the experiments. V.S.B, M.A.G, and T.H.R.N performed the research, analyzed the data, and wrote the manuscript. All authors have read and agreed to the published version of the manuscript.

Conflict of interest

The authors declare no conflict of interest.

Supporting Information

Additional experimental details and results.

Acknowledgments

This research was funded by the Joseph P. Healey Research Grant from the University of Massachusetts Boston. The authors would like to thank the Proteomics Core at the University of Massachusetts Boston for analyzing their samples on the Bruker tims-TOF HT. This work was supported in part by the National Science Foundation under grant number DMR-2338880. T.H.R.N. is supported by the National Science Foundation under grant number CMMI-2422153.

References

(1) Huang, Y.; Dong, X.; Liu, Y.; Li, L. J.; Chen, P. Graphene-Based Biosensors for Detection of Bacteria and Their Metabolic Activities. *J Mater Chem* **2011**, *21* (33), 12358–12362. https://doi.org/10.1039/c1jm11436k.

(2) Ivnitski, D.; Abdel-Hamid, I.; Atanasov, P.; Wilkins, E. Biosensors for Detection of Pathogenic Bacteria. *Biosens Bioelectron* **1999**, *14* (7), 599–624. https://doi.org/10.1016/S0956-5663(99)00039-1.

(3) Mokhtarzadeh, A.; Eivazzadeh-Keihan, R.; Pashazadeh, P.; Hejazi, M.; Gharaatifar, N.; Hasanzadeh, M.; Baradaran, B.; de la Guardia, M. Nanomaterial-Based Biosensors for Detection of Pathogenic Virus. *TrAC - Trends in Analytical Chemistry* **2017**, *97*, 445–457. https://doi.org/10.1016/j.trac.2017.10.005.

(4) Nidzworski, D.; Pranszke, P.; Grudniewska, M.; Król, E.; Gromadzka, B. Universal Biosensor for Detection of Influenza Virus. *Biosens Bioelectron* **2014**, *59*, 239–242. https://doi.org/10.1016/j.bios.2014.03.050.

(5) Nemiwal, M.; Zhang, T. C.; Kumar, D. Enzyme Immobilized Nanomaterials as Electrochemical Biosensors for Detection of Biomolecules. *Enzyme Microb Technol* **2022**, *156*, 110006. https://doi.org/10.1016/j.enzmictec.2022.110006.

(6) Kim, H. J.; Rim, J.; Jang, C. H. Liquid-Crystal-Based Immunosensor for Diagnosis of Tuberculosis in Clinical Specimens. *ACS Appl Mater Interfaces* **2017**, *9* (25), 21209–21215. https://doi.org/10.1021/acsami.7b06189.

(7) Samphao, A.; Butmee, P.; Saejueng, P.; Pukahuta, C.; Švorc, Ľ.; Kalcher, K. Monitoring of Glucose and Ethanol during Wine Fermentation by Bienzymatic Biosensor. *Journal of Electroanalytical Chemistry* **2018**, *816*, 179–188. https://doi.org/10.1016/j.jelechem.2018.03.052.

(8) Röhlen, D. L.; Pilas, J.; Dahmen, M.; Keusgen, M.; Selmer, T.; Schöning, M. J. Toward a Hybrid Biosensor System for Analysis of Organic and Volatile Fatty Acids in Fermentation Processes. *Front Chem* **2018**, *6*, 284. https://doi.org/10.3389/fchem.2018.00284.

(9) De, E. J.; Sherwood, M. B. The Paper-Disc Agar-Plate Method for the Assay of Antibiotic Substances. *J Bacteriol* **1945**, *50* (4), 459–467.

(10) Schochetman, G.; Ou, C.-Y.; Jones, W. K. Polymerase Chain Reaction. *Source: The Journal of Infectious Diseases* **1988**, *158* (6), 1154–1157.

(11) Mullis, K. B.; Ferré, F.; Gibbs, R. A. *The Polymerase Chain Reaction*; Birkhäuser: Boston, 1994.

(12) Butler, J. E. Enzyme-Linked Immunosorbent Assay. *J Immunoassay* **2000**, *21* (2–3), 165–209. https://doi.org/10.1080/01971520009349533.

(13) Oliveira, S. C.; Soares, M. S.; Gonçalves, B. V.; Rodrigues, A. C. M.; Soares, A. M. V. M.; Sobral, R. G.; Santos, N. F.; Nedoma, J.; Almeida, P. L.; Marques, C. Liquid Crystal Immunosensors for the Selective Detection of *Escherichia Coli* with a Fast Analysis Tool. *Photonics Res* **2024**, *12* (7), 1564. https://doi.org/10.1364/PRJ.524660.

(14) Collings, P. J.; Goodby, J. W. *Introduction to Liquid Crystals Chemistry and Physics*; CRC Press, 2019.

(15) Kawamoto, H. The History of Liquid-Crystal Displays. *Proceedings of the IEEE* **2002**, *90* (4), 460–500. https://doi.org/10.1109/JPROC.2002.1002521.

(16) Palffy-Muhoray, P. The Diverse World of Liquid Crystals. *Phys Today* **2007**, *60* (9), 54–60. https://doi.org/10.1063/1.2784685.

(17) Hu, X.; Zhang, X.; Yang, W.; Jiang, X.; Jiang, X.; Haan, L. T.; Yuan, D.; Zhao, W.; Zheng, N.; Jin, M.; Shui, L.; Schenning, A. P. H. J.; Zhou, G. Stable and Scalable Smart Window Based on Polymer Stabilized Liquid Crystals. *J Appl Polym Sci* **2020**, *137* (30), 48917. https://doi.org/10.1002/app.48917.

(18) Patel, J. S.; Saifi, M. A.; Berreman, D. W.; Lin, C.; Andreadakis, N.; Lee, S. D. Electrically Tunable Optical Filter for Infrared Wavelength Using Liquid Crystals in a Fabry–Perot Étalon. *Appl Phys Lett* **1990**, *57* (17), 1718–1720. https://doi.org/10.1063/1.104045.

(19) Keenan, K. E.; Stupic, K. F.; Russek, S. E.; Mirowski, E. MRI-visible Liquid Crystal Thermometer. *Magn Reson Med* **2020**, *84* (3), 1552–1563. https://doi.org/10.1002/mrm.28224.

(20) Wang, Y.; Zhao, L.; Xu, A.; Wang, L.; Zhang, L.; Liu, S.; Liu, Y.; Li, H. Detecting Enzymatic Reactions in Penicillinase via Liquid Crystal Microdroplet-Based PH Sensor. *Sens Actuators B Chem* **2018**, *258*, 1090–1098. https://doi.org/10.1016/J.SNB.2017.12.012.

(21) Kim, J.; Khan, M.; Park, S. Y. Glucose Sensor Using Liquid-Crystal Droplets Made by Microfluidics. *ACS Appl Mater Interfaces* **2013**, *5* (24), 13135–13139. https://doi.org/10.1021/AM404174N/SUPPL_FILE/AM404174N_SI_001.PDF.

(22) Bi, X.; Hartono, D.; Yang, K. L. Real-Time Liquid Crystal PH Sensor for Monitoring Enzymatic Activities of Penicillinase. *Adv Funct Mater* **2009**, *19* (23), 3760–3765. https://doi.org/10.1002/ADFM.200900823.

(23) Chen, C.-H.; Lin, Y.-C.; Chang, H.-H.; Lee, A. S.-Y. Ligand-Doped Liquid Crystal Sensor System for Detecting Mercuric Ion in Aqueous Solutions. *Anal Chem* **2015**, *87* (8), 4546–4551. https://doi.org/10.1021/acs.analchem.5b00675.

(24) Lai, Y. T.; Kuo, J. C.; Yang, Y. J. A Novel Gas Sensor Using Polymer-Dispersed Liquid Crystal Doped with Carbon Nanotubes. *Sens Actuators A Phys* **2014**, *215*, 83–88. https://doi.org/10.1016/J.SNA.2013.12.021.

(25) Wang, P. H.; Yu, J. H.; Zhao, Y. Bin; Li, Z. J.; Li, G. Q. A Novel Liquid Crystal-Based Sensor for the Real-Time Identification of Organophosphonate Vapors. *Sens Actuators B Chem* **2011**, *160* (1), 929–935. https://doi.org/10.1016/J.SNB.2011.09.005.

(26) Ma, H.; Kang, Q.; Wang, T.; Xiao, J.; Yu, L. Liquid Crystals-Based Sensor for the Detection of Lithocholic Acid Coupled with Competitive Host-Guest Inclusion. *Colloids Surf B Biointerfaces* **2019**, *173*, 178–184. https://doi.org/10.1016/j.colsurfb.2018.09.071.

(27) Huang, H. B.; Weng, G. Q.; Liang, A. H.; Jiang, Z. L. Liquid Crystal 5CB-Loaded Nanogold as New Nanocatalyst Combined with Aptamer to Determine Small Organic Pollutants by Cu2O Resonance Rayleigh Scattering Probe. *Chemical Papers* **2023**, *77* (1), 141–149. https://doi.org/10.1007/S11696-022-02456-X/METRICS.

(28) Singh, S. K.; Nandi, R.; Mishra, K.; Singh, H. K.; Singh, R. K.; Singh, B. Liquid Crystal Based Sensor System for the Real Time Detection of Mercuric Ions in Water Using Amphiphilic Dithiocarbamate. *Sens Actuators B Chem* **2016**, *226*, 381–387. https://doi.org/10.1016/J.SNB.2015.11.077.

(29) Ren, H.; An, Z.; Jang, C. H. Liquid Crystal-Based Aptamer Sensor for Sensitive Detection of Bisphenol A. *Microchemical Journal* **2019**, *146*, 1064–1071. https://doi.org/10.1016/J.MICROC.2019.02.019.

(30) Woltman, S. J.; Jay, G. D.; Crawford, G. P. Liquid-Crystal Materials Find a New Order in Biomedical Applications. *Nature Materials 2007 6:12* **2007**, *6* (12), 929–938. https://doi.org/10.1038/nmat2010.

(31) Zhai, J.; Fong, C.; Tran, N.; Drummond, C. J. Non-Lamellar Lyotropic Liquid Crystalline Lipid Nanoparticles for the Next Generation of Nanomedicine. *ACS Nano* **2019**, *13* (6), 6178–6206. https://doi.org/10.1021/acsnano.8b07961.

(32) Otón, E.; Otón, J. M.; Caño-García, M.; Escolano, J. M.; Quintana, X.; Geday, M. A. Rapid Detection of Pathogens Using Lyotropic Liquid Crystals. *Opt Express* **2019**, *27* (7), 10098. https://doi.org/10.1364/OE.27.010098.

(33) Collings, P. J.; Patel, J. S. *Handbook of Liquid Crystal Research*; Oxford University Press: Oxford, 1997.

(34) Jerome, B. Surface Effects and Anchoring in Liquid Crystals. *Reports on Progress in Physics* **1991**, *54* (3), 391–451. https://doi.org/10.1088/0034-4885/54/3/002.

(35) Chen, S.; Zhang, J.; Liu, H.; Qiu, T.; Tang, H.; Zhang, Z. Dissipative Particle Dynamics Simulation of the Sensitive Anchoring Behavior of Smectic Liquid Crystals at Aqueous Phase. *Molecules* **2022**, *27* (21), 7433. https://doi.org/10.3390/molecules27217433.

(36) Suh, A.; Gim, M.-J.; Beller, D.; Yoon, D. K. Topological Defects and Geometric Memory across the Nematic–Smectic A Liquid Crystal Phase Transition. *Soft Matter* **2019**, *15*, 5835–5841. https://doi.org/10.1039/C9SM00781D.

(37) Gupta, V. K.; Skaife, J. J.; Dubrovsky, T. B.; Abbott, N. L. Optical Amplification of Ligand-Receptor Binding Using Liquid Crystals. **1998**, *279* (5359), 2077–2080. https://doi.org/10.1126/science.279.5359.2077.

(38) Brake, J. M.; Mezera, A. D.; Abbott, N. L. Effect of Surfactant Structure on the Orientation of Liquid Crystals at Aqueous-Liquid Crystal Interfaces. *Langmuir* **2003**, *19* (16), 6436–6442. https://doi.org/10.1021/la034132s.

(39) Guzmán, O.; Abbott, N. L.; de Pablo, J. J. Quenched Disorder in a Liquid-Crystal Biosensor: Adsorbed Nanoparticles at Confining Walls. *J Chem Phys* **2005**, *122* (18), 184711. https://doi.org/10.1063/1.1896354.

(40) Lowe, A. M.; Abbott, N. L. Liquid Crystalline Materials for Biological Applications. *Chemistry of Materials* **2012**, *24* (5), 746–758. https://doi.org/10.1021/cm202632m.

(41) Carlton, R. J.; Hunter, J. T.; Miller, D. S.; Abbasi, R.; Mushenheim, P. C.; Tan, L. N.; Abbott, N. L. Chemical and Biological Sensing Using Liquid Crystals. *Liq Cryst Rev* **2013**, *1* (1), 29–51. https://doi.org/10.1080/21680396.2013.769310.

(42) Popov, N.; Honaker, L. W.; Popova, M.; Usol'tseva, N.; Mann, E. K.; Jákli, A.; Popov, P. Thermotropic Liquid Crystal-Assisted Chemical and Biological Sensors. *Materials* **2017**, *11* (1), 20. https://doi.org/10.3390/ma11010020.

(43) Pani, I.; Sil, S.; Pal, S. K. Liquid Crystal Biosensors: A New Therapeutic Window to Point-of-Care Diagnostics. *Langmuir* **2022**, *39* (3), 909–917. https://doi.org/10.1021/acs.langmuir.2c02959.

(44) Wu, P. C.; Karn, A.; Lee, M. J.; Lee, W.; Chen, C. Y. Dye-Liquid-Crystal-Based Biosensing for Quantitative Protein Assay. *Dyes and Pigments* **2018**, *150*, 73–78. https://doi.org/10.1016/j.dyepig.2017.11.013.

(45) Popov, P.; Honaker, L. W.; Kooijman, E. E.; Mann, E. K.; Jákli, A. I. A Liquid Crystal Biosensor for Specific Detection of Antigens. *Sens Biosensing Res* **2016**, *8*, 31–35. https://doi.org/10.1016/j.sbsr.2016.03.008.

(46) Wang, I.-T.; Lee, Y.-H.; Chuang, E.-Y.; Hsiao, Y.-C. Sensitive, Color-Indicating and Labeling-Free Multi-Detection Cholesteric Liquid Crystal Biosensing Chips for Detecting Albumin. *Polymers (Basel)* **2021**, *13* (9), 1463. https://doi.org/10.3390/polym13091463.

(47) Gollapelli, B.; Tatipamula, A. K.; Dewanjee, S.; Pathinti, R. S.; Vallamkondu, J. Detection of Bile Acids Using Optical Biosensors Based on Cholesteric Liquid Crystal Droplets. *J Mater Chem C Mater* **2021**, *9* (39), 13991–14002. https://doi.org/10.1039/D1TC02801D.

(48) Lee, M.-J.; Chang, C.-H.; Lee, W. Label-Free Protein Sensing by Employing Blue Phase Liquid Crystal. *Biomed Opt Express* **2017**, *8* (3), 1712. https://doi.org/10.1364/BOE.8.001712.

(49) Chen, J.; Liu, Z.; Yang, R.; Liu, M.; Yao, J.; Zhang, M.; Li, N.; Yuan, Z.; Jin, M.; Shui, L. A Label-Free Optical Immunoassay Based on Birefringence of Liquid Crystal for Insulin-like Growth Factor-I Sensing. *Sens Actuators B Chem* **2022**, *352*, 131028. https://doi.org/10.1016/j.snb.2021.131028.

(50) Popov, P.; Mann, E. K.; Jákli, A. Thermotropic Liquid Crystal Films for Biosensors and Beyond. *J Mater Chem B* **2017**, *5* (26), 5061–5078. https://doi.org/10.1039/c7tb00809k.

(51) Femmer, T.; Kuehne, A. J. C.; Wessling, M. Print Your Own Membrane: Direct Rapid Prototyping of Polydimethylsiloxane. *Lab Chip* **2014**, *14* (15), 2610. https://doi.org/10.1039/c4lc00320a.

(52) Nedoma, J.; Fajkus, M.; Siska, P.; Martinek, R.; Vasinek, V. Non-Invasive Fiber Optic Probe Encapsulated Into PolyDiMethylSiloxane for Measuring Respiratory and Heart Rate of the Human Body. *Advances in Electrical and Electronic Engineering* **2017**, *15* (1), 93–100. https://doi.org/10.15598/aeee.v15i1.1923.

(53) Nobuaki Matsuhashi; Munehiro Kimura; Tadashi Akahane; Masafumi Yoshida. Structure Analysis Of 4-Octyl-4'-Cyanobiphenyl Liquid-Crystalline Free-Standing Film By Molecular Dynamics Simulation. *The AZo Journal of Materials Online* **2007**, *3*. https://doi.org/10.2240/azojomo0234.

(54) Vahedi, A.; Kouhi, M. Liquid Crystal-Based Surface Plasmon Resonance Biosensor. *Plasmonics* **2020**, *15* (1), 61–71. https://doi.org/10.1007/s11468-019-01009-5.

(55) Lee, M.-J.; Lee, W. Liquid Crystal-Based Capacitive, Electro-Optical and Dielectric Biosensors for Protein Quantitation. *Liq Cryst* **2020**, *47* (8), 1145–1153. https://doi.org/10.1080/02678292.2019.1673908.

(56) Lopez, D.; Lauga, E. Dynamics of Swimming Bacteria at Complex Interfaces. *Physics of Fluids* **2014**, *26* (7), 071902. https://doi.org/10.1063/1.4887255.

(57) Washington, D. C. Size Limits of Very Small Microorganisms Proceedings of a Workshop Steering Group for the Workshop on Size Limits of Very Small Microorganisms Space Studies Board Commission on Physical Sciences, Mathematics, and Applications National Research Council National Academy Press. **1999**.

(58) Errington, J.; Van Der Aart, L. T. Microbe Profile: Bacillus Subtilis: Model Organism for Cellular Development, and Industrial Workhorse. *Microbiology (N Y)* **2020**, *166*, 425–427. https://doi.org/10.1099/mic.0.000922.

(59) Silhavy, T. J.; Kahne, D.; Walker, S. The Bacterial Cell Envelope. *Cold Spring Harb Perspect Biol* **2010**, *2* (5), a000414–a000414. https://doi.org/10.1101/cshperspect.a000414.

(60) Sezonov, G.; Joseleau-Petit, D.; D'Ari, R. *Escherichia Coli* Physiology in Luria-Bertani Broth. *J Bacteriol* **2007**, *189* (23), 8746–8749. https://doi.org/10.1128/JB.01368-07.

(61) Baczyński, S.; Sobotka, P.; Marchlewicz, K.; Słowikowski, M.; Juchniewicz, M.; Dybko, A.; Rutkowska, K. A. Orientation of Liquid Crystalline Molecules on Pdms Surfaces and within Pdms Microfluidic Systems. *Applied Sciences (Switzerland)* **2021**, *11* (24), 11593. https://doi.org/10.3390/app112411593.

(62) Hartono, D.; Bi, X.; Yang, K. L.; Yung, L. Y. L. An Air-Supported Liquid Crystal System for Real-Time and Label-Free Characterization of Phospholipases and Their Inhibitors. *Adv Funct Mater* **2008**, *18* (19), 2938–2945. https://doi.org/10.1002/adfm.200800424.

(63) Fournier, J. B.; Durand, G. Focal Conic Faceting in Smectic-A Liquid Crystals. *Journal de Physique II* **1991**, *1* (7), 845–870. https://doi.org/10.1051/jp2:1991113.

(64) Lavrentovich, O. D.; Kléman, M.; Pergamenshchik, V. M. Nucleation of Focal Conic Domains in Smectic A Liquid Crystals. *Journal de Physique II* **1994**, *4* (2), 377–404. https://doi.org/10.1051/jp2:1994135.

(65) Honglawan, A.; Beller, D. A.; Cavallaro, M.; Kamien, R. D.; Stebe, K. J.; Yang, S. Topographically Induced Hierarchical Assembly and Geometrical Transformation of Focal Conic Domain Arrays in Smectic Liquid Crystals. *Proc Natl Acad Sci U S A* **2013**, *110* (1), 34–39. https://doi.org/10.1073/PNAS.1214708109/-/DCSUPPLEMENTAL.

(66) Beller, D. A.; Gharbi, M. A.; Honglawan, A.; Stebe, K. J.; Yang, S.; Kamien, R. D. Focal Conic Flower Textures at Curved Interfaces. *Phys Rev X* **2013**, *3* (4), 041026. https://doi.org/10.1103/PhysRevX.3.041026.

(67) Brake, J. M.; Daschner, M. K.; Luk, Y. Y.; Abbott, N. L. Biomolecular Interactions at Phospholipid-Decorated Surfaces of Liquid Crystals. *Science (1979)* **2003**, *302* (5653), 2094–2097. https://doi.org/10.1126/SCIENCE.1091749/SUPPL_FILE/BRAKE.SOM.PDF.

(68) Chen, J.; Liu, Z.; Yang, R.; Liu, M.; Feng, H.; Li, N.; Jin, M.; Zhang, M.; Shui, L. A Liquid Crystal-Based Biosensor for Detection of Insulin Driven by Conformational Change of an Aptamer at Aqueous-Liquid Crystal Interface. *J Colloid Interface Sci* **2022**, *628*, 215–222. https://doi.org/10.1016/j.jcis.2022.07.051.

(69) Tjalsma, H.; Antelmann, H.; Jongbloed, J. D. H.; Braun, P. G.; Darmon, E.; Dorenbos, R.; Dubois, J.-Y. F.; Westers, H.; Zanen, G.; Quax, W. J.; Kuipers, O. P.; Bron, S.; Hecker, M.; van Dijl, J. M. Proteomics of Protein Secretion by Bacillus Subtilis : Separating the "Secrets" of the Secretome . *Microbiology and Molecular Biology Reviews* **2004**, *68* (2), 207–233. https://doi.org/10.1128/mmbr.68.2.207-233.2004.

(70) Monteiro, R.; Chafsey, I.; Ageorges, V.; Leroy, S.; Chambon, C.; Hébraud, M.; Livrelli, V.; Pizza, M.; Pezzicoli, A.; Desvaux, M. The Secretome Landscape of Escherichia Coli O157:H7: Deciphering the Cell-Surface, Outer Membrane Vesicle and Extracellular Subproteomes. *J Proteomics* **2021**, *232*, 104025. https://doi.org/10.1016/j.jprot.2020.104025.

(71) Boysen, A.; Borch, J.; Krogh, T. J.; Hjernø, K.; Møller-Jensen, J. SILAC-Based Comparative Analysis of Pathogenic Escherichia Coli Secretomes. *J Microbiol Methods* **2015**, *116*, 66–79. https://doi.org/10.1016/j.mimet.2015.06.015.

(72) Falcón García, C.; Kretschmer, M.; Lozano-Andrade, C. N.; Schönleitner, M.; Dragoŝ, A.; Kovács, Á. T.; Lieleg, O. Metal Ions Weaken the Hydrophobicity and Antibiotic Resistance of Bacillus Subtilis NCIB 3610 Biofilms. *npj Biofilms and Microbiomes 2020 6:1* **2020**, *6* (1), 1–11. https://doi.org/10.1038/s41522-019-0111-8.

(73) Hobley, L.; Ostrowski, A.; Rao, F. V.; Bromley, K. M.; Porter, M.; Prescott, A. R.; MacPhee, C. E.; van Aalten, D. M. F.; Stanley-Wall, N. R. BslA Is a Self-Assembling Bacterial Hydrophobin That Coats the *Bacillus Subtilis* Biofilm. *Proceedings of the National Academy of Sciences* **2013**, *110* (33), 13600–13605. https://doi.org/10.1073/pnas.1306390110.

(74) Iglesias, W.; Abbott, N. L.; Mann, E. K.; Jákli, A. Improving Liquid-Crystal-Based Biosensing in Aqueous Phases. *ACS Appl Mater Interfaces* **2012**, *4* (12), 6884–6890. https://doi.org/10.1021/am301952f.

(75) Schindelin, J.; Arganda-Carreras, I.; Frise, E.; Kaynig, V.; Longair, M.; Pietzsch, T.; Preibisch, S.; Rueden, C.; Saalfeld, S.; Schmid, B.; Tinevez, J.-Y.; White, D. J.; Hartenstein, V.; Eliceiri, K.; Tomancak, P.; Cardona, A. Fiji: An Open-Source Platform for Biological-Image Analysis. *Nat Methods* **2012**, *9* (7), 676–682. https://doi.org/10.1038/nmeth.2019.

Smectic LC biosensor for the detection of biomolecules

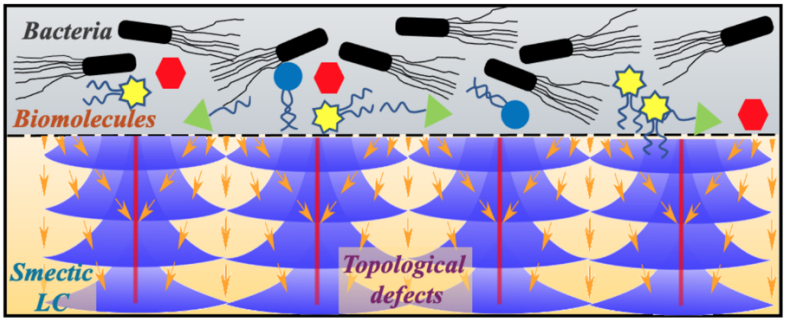

TOC: Smectic LC biosensor for the detection of biomolecules

Supporting Information

Biosensing of Bacterial Secretions via Topological Defects at Smectic Interfaces

*Vajra S. Badha,[a] Tagbo H.R. Niepa,[b,c] and Mohamed Amine Gharbi[a]**

[a] Department of Physics, University of Massachusetts Boston, Boston, MA 02125, USA

[b] Department of Chemical Engineering, Carnegie Mellon University, Pittsburgh, PA 15213, USA

[c] Department of Biomedical Engineering, Carnegie Mellon University, Pittsburgh, PA 15213, USA

Effect of the liquid crystal on the PDMS

To ensure that 4′-octyl-4-biphenylcarbonitrile (8CB) liquid crystal (LC) does not alter the shape of polydimethylsiloxane (PDMS) holes during the experiment, we prepared a sample with 8CB and terrific broth (TB) and observed it under a microscope for 50 minutes, capturing images every minute. The goal was to verify if PDMS changes shape when interacting with 8CB, which could impact the interaction of bacteria with the LC interface. Throughout the

observation period (~ 50 minutes), no significant changes were detected in the shape of the PDMS holes or the properties of focal conic domains (FCDs), particularly those located far from the boundaries. This confirms that the structural changes in defects observed at the LC interface are due to the interaction between TB and the smectic interface, not due to any alteration in PDMS shape. Our data confirms that PDMS maintains its properties over the duration of our investigations.

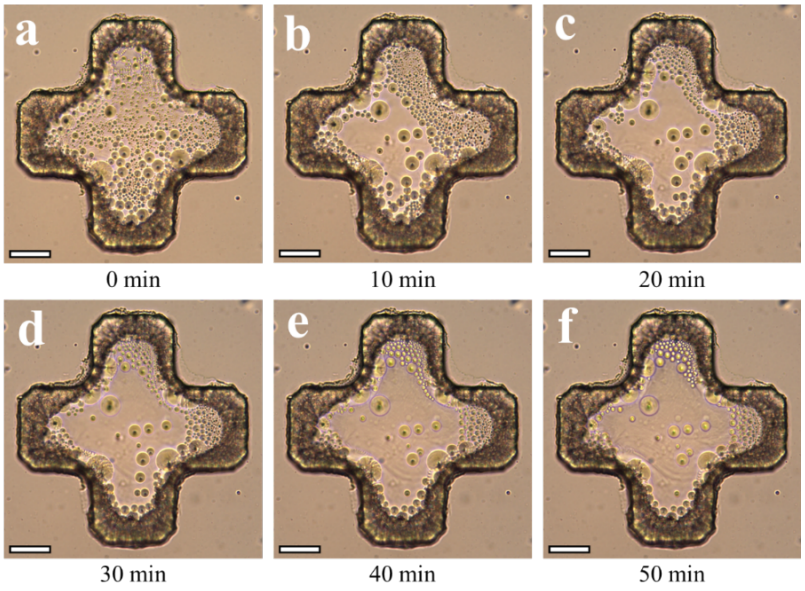

Figure S1: Effect of the 8CB on the shape of PDMS. The images **a-f** represent the timeline over a period of 50 minutes. The scale bars are 50 μm.

Protocol of the Bicinchoninic Acid (BCA) Assay

To better understand the interaction between the smectic interface and *Escherichia coli* (*E. coli*) or *Bacillus subtilis* (*B. subtilis*) cells, and to investigate the underlying reason for the smectic LC's difference in response to different bacteria, we used a Bruker tims-TOF HT mass spectrometer to

conduct a BCA proteomics assay and identify the protein secretions in their solutions. After preparing the extracted protein samples, an aliquot of 100 µg of each sample was extracted and 20 µL of 500 mM ammonium bicarbonate was added to each sample. The volumes were all brought up to 100 µL with Optima water, bringing the final concentration of ammonium bicarbonate to 100 mM. The samples were reduced with 2.1 µL of 500 mM dithiothreitol (DTT) for 45-mintes at 60 °C, and then cooled to room temperature before being alkylated with 11.5 µL of 500 mM iodoacetamide (IAA), in the dark, for 30-minutes. The samples were then digested with 2.5 µL of 1 mg/mL of Trypsin/Lys-C overnight at 37 °C.

Liquid Chromatography with Ion Mobility – Mass Spectrometry (LC-IM-MS): The samples were run on an Evosep One nLC (Evosep, Odense, Denmark) coupled to a Bruker timsTOF HT mass spectrometer (Bruker Scientific LLC, Billerica, MA) on a PepSep Endurance column (15 cm x 15 cm, 1.9 µm) (PepSep, Odense, Denmark) and operated in Parallel Accumulation – Serial Fragmentation (PASEF) mode with a scan range of 100-1700 m/z and a mobility range of 0.60-1.60 $V \cdot s/cm^3$. The ramp time and accumulation times were both set to 100.0 ms, while the ramp rate to 9.42 Hz, and the MS averaging to 1. For the MS/MS parameters, the number of PASEF ramps was set to 10 with a total cycle time of 1.17 s with a target intensity of 10000 and the intensity threshold of 2500.

Data Analysis: Protein identification and quantification analysis were done with Parallel database Search Engine in Real-Time (PaSER, 2023, v 3.0, Bruker Scientific LLC, Billerica, MA) using ProLuCID,[1] DTASelect2[2,3] and Census.[4,5] Mass spectra were searched against Uniprot Escherichia_coli and Bacillus_subtilis up-to-date protein databases plus sequences of known contaminants such as keratin and porcine trypsin concatenated to a decoy database. TIMScore was appended to raw search results to use the peptide Collisional Cross Section (CCS) during the

validation process.[6] These search results were validated, assembled, and filtered using the DTASelect program (version 2.1).

Label Free Analysis: A label-free quantitative analysis was performed using Census through PaSER (2023, v 3.0, Bruker Scientific LLC, Billerica, MA, http://www.bruker.com). The Census used protein identification results from DTASelect2 and generated a reconstructed MS1-based extracted ion chromatograms for each identified peptide. When peptides are not identified in all the relevant samples, Census went through spectra, searching them using accurate precursor mass, retention time, ion mobility and charge states in order to retrieve them and build chromatograms.[7]

Results from the BCA assay

Below are the tables with the list of proteins identified in the BCA assay from the *E. coli* and *B. subtilis* protein solutions obtained by removing the bacteria from the overnight cultures obtained.

Table S1. Total Proteins in the *E. coli* overnight growth solution.

1	Flagellin
2	Chaperone protein DnaK
3	2,3,4,5-tetrahydropyridine-2,6-dicarboxylate N-succinyltransferase
4	2,3-bisphosphoglycerate-dependent phosphoglycerate mutase (GN=gpmA)
5	2,3-bisphosphoglycerate-independent phosphoglycerate mutase (GN=gpmI)
6	2-dehydro-3-deoxyphosphooctonate aldolase
7	2Fe-2S ferredoxin
8	2-hydroxy-3-oxopropionate reductase
9	30S ribosomal protein S1 OX=83333

10	30S ribosomal protein S1 OX=562
11	30S ribosomal protein S10
12	30S ribosomal protein S11
13	30S ribosomal protein S13
14	30S ribosomal protein S16
15	30S ribosomal protein S18
16	30S ribosomal protein S2
17	30S ribosomal protein S21
18	30S ribosomal protein S3
19	30S ribosomal protein S4
20	30S ribosomal protein S5
21	30S ribosomal protein S6
22	30S ribosomal protein S7
23	30S ribosomal protein S7
24	30S ribosomal protein S8
25	3-mercaptopyruvate sulfurtransferase
26	3-oxoacyl-[acyl-carrier-protein] synthase 1
27	3-phenylpropionate dioxygenase beta subunit
28	4-hydroxy-tetrahydrodipicolinate synthase
29	50S ribosomal protein L1
30	50S ribosomal protein L10
31	50S ribosomal protein L14 GN=rplN
32	50S ribosomal protein L14 GN=rplO

33	50S ribosomal protein L15
34	50S ribosomal protein L16
35	50S ribosomal protein L17
36	50S ribosomal protein L19
37	50S ribosomal protein L2
38	50S ribosomal protein L21
39	50S ribosomal protein L24
40	50S ribosomal protein L25
41	50S ribosomal protein L27
42	50S ribosomal protein L28
43	50S ribosomal protein L3
44	50S ribosomal protein L31
45	50S ribosomal protein L32
46	50S ribosomal protein L4
47	50S ribosomal protein L5
48	50S ribosomal protein L6
49	50S ribosomal protein L7/L12
50	50S ribosomal protein L9
51	5-methyltetrahydropteroyltriglutamate--homocysteine methyltransferase
52	5-methyltetrahydropteroyltriglutamate—homocysteine S-methyltransferase (Fragment) GN=D3C88_21865
53	5-methyltetrahydropteroyltriglutamate--homocysteine S-methyltransferase (Fragment) GN=E4K51_29170

54	6-phosphogluconate dehydrogenase, decarboxylating
55	Acetate OX=562
56	Acetate kinase OX=83333
57	Acetyl-coenzyme A carboxylase carboxyl transferase subunit alpha
58	Acid stress chaperone HdeA
59	Acid stress chaperone HdeB
60	Acidic protein MsyB
61	Aconitate hydratase B
62	Acyl carrier protein OX=562
63	Acyl carrier protein O139:H28
64	Adenylate kinase
65	Adenylosuccinate synthetase
66	ADP-L-glycero-D-manno-heptose-6-epimerase
67	Aerobic glycerol-3-phosphate dehydrogenase
68	Aldehyde-alcohol dehydrogenase
69	Alkyl hydroperoxide reductase C
70	Alkyl hydroperoxide reductase subunit F
71	Aminoimidazole riboside kinase
72	Aminotransferase class III-fold pyridoxal phosphate-dependent enzyme
73	Anaerobic glycerol-3-phosphate dehydrogenase subunit A
74	Anaerobic glycerol-3-phosphate dehydrogenase subunit B
75	Anaerobic glycerol-3-phosphate dehydrogenase subunit B
76	Anaerobic glycerol-3-phosphate dehydrogenase subunit C

77	Anti-sigma-28 factor FlgM (Fragment)
78	Asparagine--tRNA ligase
79	Aspartate aminotransferase
80	Aspartate ammonia-lyase
81	Aspartate-semialdehyde dehydrogenase
82	ATP synthase subunit alpha
83	ATP-cone domain-containing protein
84	ATP-dependent Clp protease ATP-binding subunit ClpX
85	ATP-dependent protease ATPase subunit HslU
86	ATP-dependent protease subunit HslV
87	Autonomous glycyl radical cofactor
88	Bacterial non-heme ferritin
89	Bacterioferritin
90	Basal-body rod modification protein FlgD OX=562
91	Basal-body rod modification protein FlgD OX=83333
92	Bifunctional aldehyde-alcohol dehydrogenase AdhE
93	Bifunctional aspartokinase/homoserine dehydrogenase 1
94	Bifunctional NADP-dependent 3-hydroxy acid dehydrogenase/3-hydroxypropionate dehydrogenase YdfG
95	Catalase-peroxidase
96	Cell division protein FtsZ
97	Cell division protein ZapB
98	Cell shape-determining protein MreB

99	Chaperedoxin
100	Chaperone protein ClpB
101	Chaperone protein DnaK (Heat shock protein 70) (Heat shock 70 kDaprotein) (HSP70)
102	Chaperone protein DnaK (Heat shock protein 70) (Heat shock 70 kDaprotein) (HSP70)
103	Chaperone protein HtpG
104	Chaperone protein Skp
105	Chaperonin GroEL
106	Chaperonin GroEL 1
107	Chemotaxis protein CheW
108	Chemotaxis protein CheY
109	Citrate synthase
110	Co-chaperonin GroES
111	Cold shock-like protein CspC
112	Cold shock-like protein CspE
113	CTP synthase
114	Curved DNA-binding protein
115	Cysteine desulfurase IscS
116	Cysteine synthase
117	Cystine transporter subunit
118	Cytidine deaminase
119	Cytochrome bd-I ubiquinol oxidase subunit 1
120	Cytosol non-specific dipeptidase
121	Deoxyribose-phosphate aldolase OX=316385

122	deoxyribose-phosphate aldolase OX=562
123	D-galactose/methyl-galactoside binding periplasmic protein MglB
124	Dihydrolipoamide acetyltransferase component of pyruvate dehydrogenase complex
125	Dihydrolipoyl dehydrogenase
126	Dihydrolipoyllysine-residue acetyltransferase component of pyruvate dehydrogenase complex
127	Dihydrolipoyllysine-residue succinyltransferase component of 2-oxoglutarate dehydrogenase complex
128	Dihydroxyacetone kinase subunit K
129	Dimethyl sulfoxide reductase DmsA
130	Dipeptide-binding protein
131	DNA gyrase subunit B
132	DNA protection during starvation protein
133	DNA-binding protein HU-alpha
134	DNA-binding protein HU-beta
135	DNA-binding transcriptional dual regulator CRP
136	DNA-directed RNA polymerase subunit alpha
137	DNA-directed RNA polymerase subunit beta O1:K1
138	DNA-directed RNA polymerase subunit beta OX=562
139	DNA-directed RNA polymerase subunit beta' O1:K1
140	DNA-directed RNA polymerase subunit beta' OX=562
141	DNA-directed RNA polymerase subunit omega
142	D-tagatose-1,6-bisphosphate aldolase subunit GatY

143	D-tagatose-1,6-bisphosphate aldolase subunit GatZ
144	DUF2786 domain-containing protein
145	Ecotin
146	Elongation factor 4
147	Elongation factor G
148	Elongation factor Ts
149	Elongation factor Tu
150	Elongation factor Tu (Fragment)
151	Elongation factor Tu 1
152	Elongation protein Tu GTP binding domain-containing protein (Fragment)
153	Enolase
154	Enoyl-[acyl-carrier-protein] reductase [NADH] FabI
155	Entericidin B
156	Exonuclease SbcC
157	Fe/S biogenesis protein NfuA
158	Fimbrial family protein
159	FKBP-type 22 kDa peptidyl-prolyl cis-trans isomerase
160	FKBP-type peptidyl-prolyl cis-trans isomerase FkpA
161	FKBP-type peptidyl-prolyl cis-trans isomerase SlyD
162	Flagellar basal body rod protein FlgB
163	Flagellar hook protein FlgE
164	Flagellar hook-associated protein 1 OX=562
165	Flagellar hook-associated protein 1 OX=83333

166	Flagellar hook-associated protein 1 OX=562
167	Flagellar hook-associated protein 2
168	Flagellar hook-associated protein 3 OX=83333
169	Flagellar hook-associated protein 3 OX=562
170	Flagellin
171	Flagellin (Fragment) GN=fliC
172	Flagellin (Fragment) GN=fllA55
173	Flagellin (Fragment) GN=flnA
174	Flagellin (Fragment) GN=fliC
175	Flagellin FliC
176	Formate acetyltransferase 1
177	Fructose-1,6-bisphosphatase class 1
178	Fructose-bisphosphate aldolase class 1
179	Fructose-bisphosphate aldolase class 2
180	Fumarate hydratase class I
181	Fumarate hydratase class I, anaerobic
182	Fumarate reductase flavoprotein subunit OX=83333
183	Fumarate reductase flavoprotein subunit OX=562
184	GapA (Fragment)
185	Glucose-1-phosphatase
186	Glucose-6-phosphate isomerase
187	Glutamate decarboxylase D3G36_07530
188	glutamate decarboxylase GN=CCV24_003315

189	Glutamate decarboxylase (Fragment) GN=ACN68_06885
190	glutamate decarboxylase (Fragment) GN=DTM45_28360
191	glutamate decarboxylase (Fragment) GN=GNW61_08045
192	glutamate decarboxylase (Fragment) GN=FPI65_32745
193	Glutamate decarboxylase (Fragment) GN=ELX76_24345
194	Glutamate decarboxylase alpha
195	Glutamate/gamma-aminobutyrate antiporter
196	Glutamate--tRNA ligase
197	Glutamine-binding periplasmic protein
198	Glutaredoxin 2
199	Glutaredoxin 3
200	Glutaredoxin 4
201	Glyceraldehyde-3-phosphate dehydrogenase A
202	Glycerol kinase
203	Glycerol-3-phosphate transporter
204	Glycerophosphodiester phosphodiesterase
205	Glycerophosphodiester phosphodiesterase, periplasmic
206	Glycine--tRNA ligase beta subunit
207	Glycogen synthase
208	Glyoxalase ElbB
209	HAMP domain-containing protein (Fragment)
210	High-affinity zinc uptake system protein ZnuA
211	Histidine ABC transporter substrate-binding protein HisJ

212	Histidine phosphatase family protein
213	HlyD-family secretion protein
214	Hydrogenase-1 large chain
215	Inorganic pyrophosphatase
216	Inosine-5'-monophosphate dehydrogenase
217	Iron-containing alcohol dehydrogenase
218	Isocitrate dehydrogenase [NADP] OX=83333
219	Isocitrate dehydrogenase [NADP] (Fragment) OX=562
220	Isocitrate dehydrogenase [NADP] (Fragment) OX=562
221	Isocitrate lyase
222	Isoleucine--tRNA ligase
223	KHG/KDPG aldolase
224	L-asparaginase 2
225	L-cystine-binding protein TcyJ
226	Leu/Ile/Val-binding protein
227	Leucine--tRNA ligase
228	L-fucose mutarotase
229	Lipid A core - O-antigen ligase and related enzymes
230	Lon protease
231	Lysine/arginine/ornithine ABC transporter substrate-binding protein ArgT
232	Lysine--tRNA ligase OX=83333
233	Lysine--tRNA ligase O6:K15:H31
234	Lysine--tRNA ligase, heat inducible

235	Lysozyme
236	Major outer membrane lipoprotein Lpp
237	Malate dehydrogenase
238	Maltodextrin-binding protein (Fragment)
239	Maltose/maltodextrin-binding periplasmic protein
240	Mannitol-1-phosphate 5-dehydrogenase
241	Metal-binding protein ZinT
242	Methyl-accepting chemotaxis protein II
243	Methylated-DNA--[protein]-cysteine S-methyltransferase
244	Molecular chaperone
245	Molybdate-binding periplasmic protein
246	Molybdate-binding protein ModA
247	Molybdenum cofactor biosynthesis protein B
248	Molybdopterin guanine dinucleotide synthesis B family protein
249	Multidrug efflux pump subunit AcrA
250	NAD(P)H dehydrogenase (quinone)
251	Negative regulator of flagellin synthesis OX=562
252	Negative regulator of flagellin synthesis OX=83333
253	NH(3)-dependent NAD(+) synthetase
254	Oligopeptide ABC transporter substrate-binding protein
255	Outer membrane lipoprotein DolP
256	Outer membrane lipoprotein Slp
257	Outer membrane protein A

258	Outer membrane protein Slp
259	Outer-membrane lipoprotein carrier protein
260	Oxygen-insensitive NAD(P)H nitroreductase
261	PEP-dependent dihydroxyacetone kinase, ADP-binding subunit DhaL
262	PEP-dependent dihydroxyacetone kinase, dihydroxyacetone-binding subunit DhaK
263	PEP-dependent dihydroxyacetone kinase, phosphoryl donor subunit DhaM
264	Peptidoglycan-associated lipoprotein
265	PerC family transcriptional regulator
266	Peroxiredoxin
267	Phosphate acetyltransferase
268	Phosphocarrier protein HPr
269	Phosphoenolpyruvate carboxykinase (ATP) O1:K1
270	Phosphoenolpyruvate carboxykinase (ATP) OX=562
271	Phosphoenolpyruvate-protein phosphotransferase
272	Phosphoglycerate kinase
273	Phosphoglycerate mutase (2,3-diphosphoglycerate-independent) (Fragment)
274	Phosphopentomutase
275	Polyribonucleotide nucleotidyltransferase
276	Potassium binding protein Kbp
277	Protein disaggregation chaperone
278	Protein FlxA
279	Protein GrpE
280	Protein transport protein HofC

281	Protein YciN
282	Protein YdgH
283	Protein YgiW
284	protein-secreting ATPase (Fragment)
285	PTS system glucose-specific EIIA component
286	PTS system mannose-specific EIIAB component
287	Purine nucleoside phosphorylase DeoD-type
288	Putative Fe-S oxidoreductases (SAM domain protein)
289	Putative glucose-6-phosphate 1-epimerase
290	Putative monooxygenase YdhR
291	Putative NAD(P)H nitroreductase YdjA
292	Putative selenoprotein YdfZ
293	Pyruvate dehydrogenase E1 component
294	Pyruvate kinase I
295	Pyruvate kinase II
296	Respiratory nitrate reductase 1 alpha chain
297	Ribonuclease E
298	Ribose import binding protein RbsB
299	ribose-5-phosphate isomerase (Fragment)
300	Ribose-phosphate pyrophosphokinase
301	Ribosome-associated inhibitor A
302	Ribosome-recycling factor
303	RNA polymerase-binding transcription factor DksA

304	Sec translocon accessory complex subunit YajC
305	Selenide, water dikinase
306	Septum site-determining protein MinD
307	Serine--tRNA ligase
308	Small-conductance mechanosensitive channel
309	Stringent starvation protein A
310	Substrate-binding domain-containing protein (Fragment)
311	succinate dehydrogenase
312	Superoxide dismutase [Fe]
313	Thiol peroxidase
314	Thioredoxin 1
315	Thiosulfate-binding protein
316	Threonine--tRNA ligase
317	TIGR03756 family integrating conjugative element protein
318	Transaldolase GN=tal2
319	Transaldolase GN=tal
320	Transaldolase OX=679206
321	Transcription elongation factor GreA
322	Transcription termination/antitermination protein NusA
323	Transcription termination/antitermination protein NusG
324	Transketolase GN=tktA_3
325	Transketolase GN=tktA_1
326	Transketolase (Fragment)

327	Transketolase 1
328	Translation elongation factor G
329	Translation initiation factor IF-1
330	Translation initiation factor IF-3
331	Trehalose-6-phosphate hydrolase
332	Trigger factor O1:K1
333	Trigger factor OX=562
334	Triosephosphate isomerase
335	tRNA-dihydrouridine synthase B
336	Tryptophanase O139:H28
337	Tryptophanase OX=344610
338	Uncharacterized lipoprotein YbaY
339	Uncharacterized protein GN=C9E67_19705
340	Uncharacterized protein GN=EL79_5186
341	Uncharacterized protein GN=BANRA_05067
342	Uncharacterized protein OX=1268991 GN=HMPREF1604_00196
343	Uncharacterized protein (Fragment)
344	Uncharacterized protein Yah
345	Uncharacterized protein YccJ
346	Uncharacterized protein YjeI
347	Uncharacterized protein YncE
348	Uncharacterized protein YnfD
349	Uncharacterized protein YqjD

350	Universal stress protein F
351	UPF0149 protein YgfB
352	UPF0227 protein YcfP
353	UPF0234 protein YajQ
354	UPF0304 protein YfbU
355	UPF0325 protein YaeH
356	UPF0381 protein YfcZ
357	UPF0434 protein YcaR
358	Uracil phosphoribosyltransferase
359	Uridine phosphorylase OX=83333
360	Uridine phosphorylase OX=562
361	YgiW/YdeI family stress tolerance OB fold protein

Table S2. Total Proteins in the *B. subtilis* overnight growth solution

1	(R,R)-butanediol dehydrogenase
2	2-hydroxy-3-keto-5-methylthiopentenyl-1-phosphate phosphatase
3	30S ribosomal protein S1 homolog
4	30S ribosomal protein S2
5	30S ribosomal protein S7
6	Acetolactate synthase
7	Adenylate kinase
8	Alkyl hydroperoxide reductase C

9	Asparagine synthetase [glutamine-hydrolyzing] 1
10	ATP synthase subunit alpha
11	Cell wall-associated protease
12	Chaperone protein DnaK
13	Cold shock protein CspD
14	Cryptic catabolic NAD-specific glutamate dehydrogenase GudB
15	D-alanyl carrier protein
16	DNA gyrase subunit A
17	DNA processing protein DprA
18	DNA-binding protein HU 1
19	Ferredoxin
20	Flagellar M-ring protein
21	Flagellin
22	Glutamate synthase [NADPH] large chain
23	Glutamine synthetase
24	Glycerol kinase
25	Heme-degrading monooxygenase HmoB
26	Immunity protein YezG
27	Inosine-5'-monophosphate dehydrogenase
28	Isoleucine--tRNA ligase
29	Lactate utilization protein C
30	L-Ala-D/L-Glu epimerase
31	Malate dehydrogenase

32	Methionine-binding lipoprotein MetQ
33	NAD-dependent malic enzyme 1
34	Negative regulator of genetic competence ClpC/MecB
35	Nuclease SbcCD subunit C
36	Ornithine aminotransferase
37	Penicillin-binding protein 1A/1B
38	Phage-like element PBSX protein XkdF
39	Phosphoglycerate kinase
40	Polyketide synthase PksJ
41	Polyribonucleotide nucleotidyltransferase
42	Probable cytosol aminopeptidase
43	Protein translocase subunit SecA
44	Purine nucleoside phosphorylase 1
45	Putative cell wall shaping protein YabE
46	Putative cytochrome P450 YjiB
47	Putative nitrogen fixation protein YutI
48	Putative tRNA-binding protein YtpR
49	Pyruvate dehydrogenase E1 component subunit alpha
50	Ribonucleoside-diphosphate reductase subunit beta
51	Ribosome biogenesis GTPase A
52	Ribosome-recycling factor
53	S-adenosylmethionine synthase
54	Serine protease Do-like HtrA

55	SPbeta prophage-derived stress response protein SCP1
56	Sporulation kinase A
57	Succinate dehydrogenase flavoprotein subunit
58	Superoxide dismutase [Mn]
59	Thioredoxin
60	Toxin YqcG
61	Transcription termination/antitermination protein NusA
62	Transcription termination/antitermination protein NusG
63	Transcriptional regulatory protein ResD
64	Trifunctional nucleotide phosphoesterase protein YfkN
65	Trigger factor
66	tRNA nuclease WapA
67	tRNA-2-methylthio-N(6)-dimethylallyladenosine synthase
68	Uncharacterized phosphotransferase YvkC
69	Uncharacterized protein YceE
70	Uncharacterized protein YncM
71	Uncharacterized protein YneR
72	Uncharacterized protein YppF
73	Uncharacterized protein YqjE
74	Uncharacterized protein YwoF
75	UPF0702 transmembrane protein YdfS
76	Vegetative catalase
77	Vegetative protein 296

Table S3. Proteins identified in both the *E. coli* and *B. subtilis* overnight growth solutions

1	30S ribosomal protein S1 homolog
2	30S ribosomal protein S7
3	Adenylate kinase
4	Alkyl hydroperoxide reductase C
5	ATP synthase subunit alpha
6	Chaperone protein DnaK
7	Cold shock protein CspD
8	Flagellin
9	Glycerol kinase
10	Inosine-5'-monophosphate dehydrogenase
11	Isoleucine--tRNA ligase
12	Malate dehydrogenase
13	Phosphoglycerate kinase
14	Polyribonucleotide nucleotidyltransferase
15	Pyruvate dehydrogenase E1 component subunit alpha
16	Ribosome-recycling factor
17	Thioredoxin

18	Transcription termination/antitermination protein NusA
19	Transcription termination/antitermination protein NusG
20	Trigger factor

Table S4. Lipoproteins identified in the *E. coli* solution.

1	Major outer membrane lipoprotein Lpp
2	Outer membrane lipoprotein DolP
3	Outer membrane lipoprotein Slp 1
4	Outer membrane lipoprotein Slp 2
5	Outer-membrane lipoprotein carrier protein
6	Peptidoglycan-associated lipoprotein
7	Uncharacterized lipoprotein YbaY

Table S5. Lipoproteins identified in the *B. subtilis* solution.

1	Methionine-binding lipoprotein MetQ

Estimation of Bacterial concentration using image analysis

To measure the bacterial concentration of the sample at the time of capturing images, we select a 50 µm x 50 µm region in the image captured for the optical analysis. Subsequently, the number of bacteria in the selected region are counted using the multi-point tool of ImageJ **(Figure S2)**. As the height of the experimental setup was fixed at 25 µm using spacers, the number of bacteria counted represented the bacteria in 50 x 50 x 25 μm^3 volume (6.25 x 10-8 mL). We then extrapolated this number counted in 6.25 x 10-8 mL to 1 mL and obtained the estimated bacterial concentration per mL. This process was repeated 6 times by selecting different regions in the image randomly for each sample to obtain an average, standard deviation, and standard error. The results are shown below in **Table S6**.

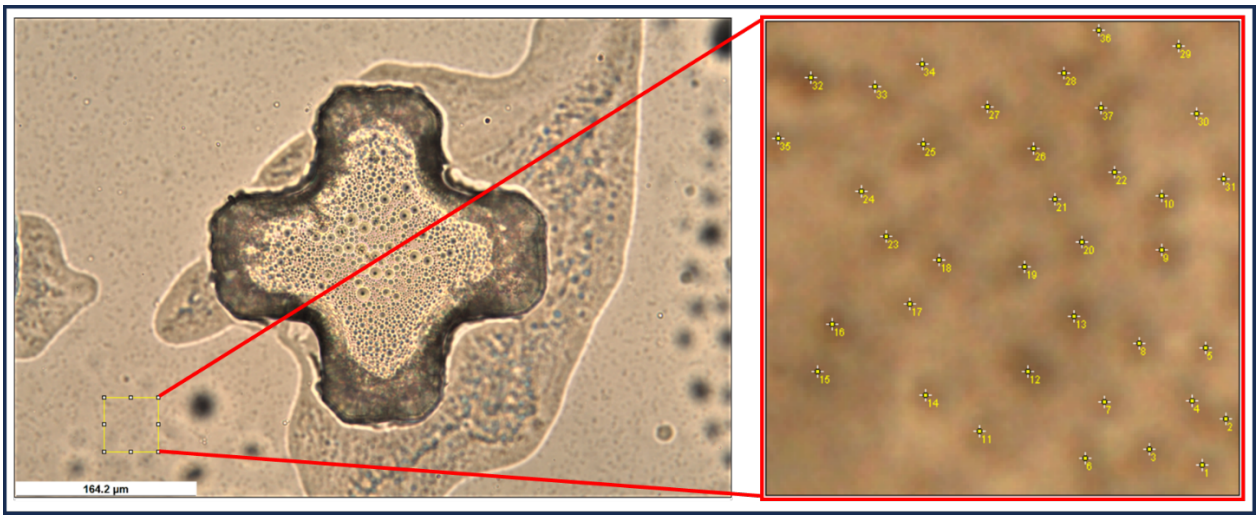

Figure S2. The above figure illustrates the bacteria counting process. A region measuring 50 µm x 50 µm is chosen randomly, and the number of bacteria is counted using the image processing software FIJI. The scale bar is 164.2 µm.

Table S6. Measuring the average concentration of bacteria in different samples.

	Sample 02	**Sample 02**	**Sample 02**	**Sample 02**	**Sample 02**	**Sample 02**
	(x 10^9)	**(x 10^9)**	**(x 10^9)**	**(x 10^9)**	**(x 10^9)**	**(x 10^9)**
Count 1	0.672	0.976	1.60	1.60	2.19	3.30
Count 2	0.608	1.02	1.39	1.70	2.26	3.04
Count 3	0.560	1.02	1.58	1.73	1.97	2.96
Count 4	0.576	0.944	1.49	1.66	2.82	3.09
Count 5	0.560	0.976	1.71	1.70	2.42	2.80
Count 6	0.624	0.960	1.41	1.63	2.10	3.23
Average	0.600	0.984	1.53	1.67	2.29	3.07
Standard Deviation	0.040	0.030	0.113	0.043	0.272	0.165
Standard Error	0.016	0.012	0.046	0.017	0.111	0.067

*All the values are in cells/mL

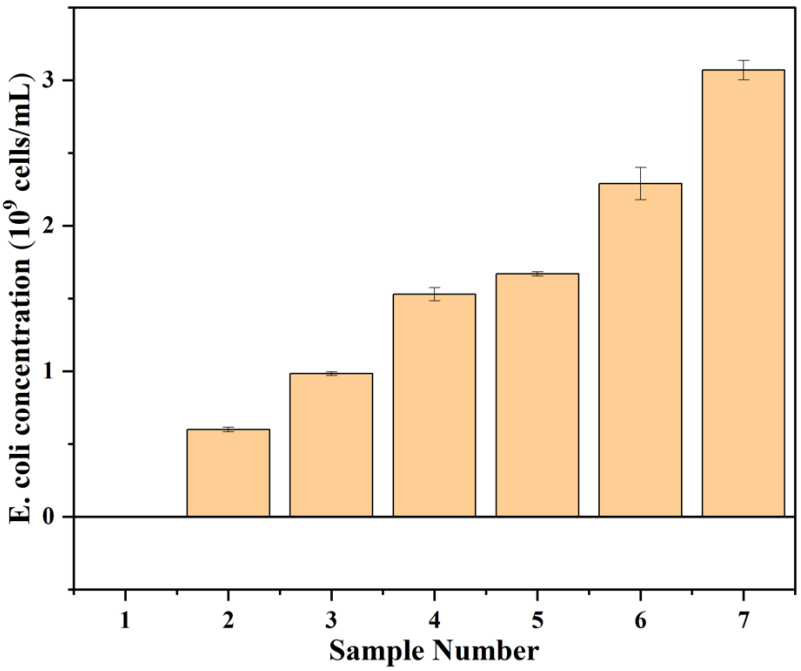

Figure S3: Bacterial concentrations estimated using image processing technique. Sample 1 is a negative control (Sterile TB).

From **Table S6** and **Figure S3**, we confirm that the standard deviation, standard error, and percent error of estimation using the image processing technique are very low in comparison to the average values. The R^2 value was 0.98.

Measuring the average FCD sizes at the interface

To measure the average FCD size at the interface, the images obtained from optical microscopy were transferred to FIJI, and the areas of individual FCDs were measured using the oval tool.

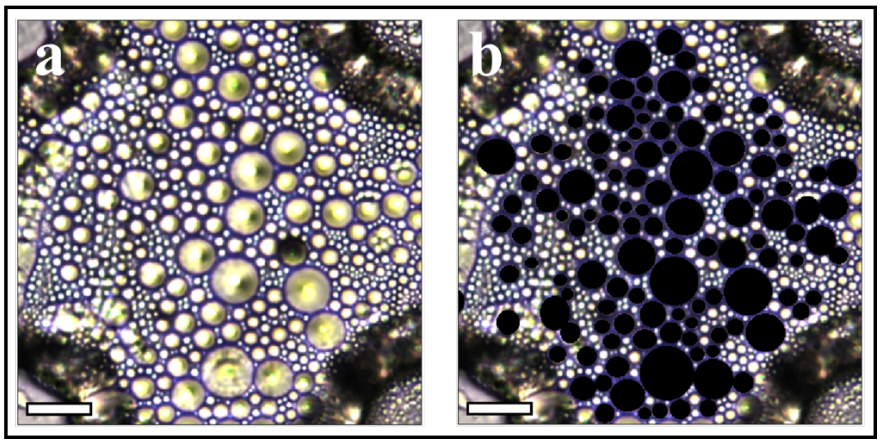

Figure S4: Method used to measure the average size of FCDs. (a) Image of FCDs before the analysis. (b) Image of FCDs after the analysis. The dark regions show the areas considered, which are larger than 30 μm^2. The scale bar is 25 μm.

Comparison of bacteria concentration – Optical density method vs. image processing technique

To support our protocol of estimating the bacterial concentration, we conducted a study to compare the concentrations of *E. coli* bacteria obtained using optical density measured at 600 nm wavelength (OD_{600}), with the concentrations estimated using FIJI analysis (see Material and Methods 2.5). Overnight (~14 hours) *E. coli* culture was diluted serially to prepare different concentrations of the bacterial solution. The OD_{600} measurement for these solutions was measured using a spectrometer (Agilent Cary 60 UV-VIS). Then, 15 μL of the bacterial solution was immediately transferred onto the experimental sample and, subsequently, the sample onto the

microscope to capture the image. The images were transferred to FIJI to estimate the concentration of bacteria.

Table S7. Average concentration of bacteria using FIJI, for different OD_{600} measurements.

	OD = 0.97	**0.57**	**0.37**	**0.27**	**0.18**
	(x 10^9)	**(x 10^9)**	**(x 10^9)**	**(x 10^9)**	**(x 10^9)**
Count 1	3.46	0.832	0.720	0.336	0.224
Count 2	2.93	0.752	0.880	0.416	0.208
Count 3	3.34	0.784	0.784	0.352	0.224
Count 4	3.92	0.688	0.896	0.400	0.256
Count 5	3.18	0.784	0.816	0.400	0.304
Count 6	3.07	0.928	0.784	0.352	0.224
Average	3.32	0.795	0.813	0.376	0.240
Standard Deviation	0.320	0.074	0.060	0.030	0.032
Standard Error	0.130	0.030	0.025	0.012	0.013

*All the values are in cells/mL

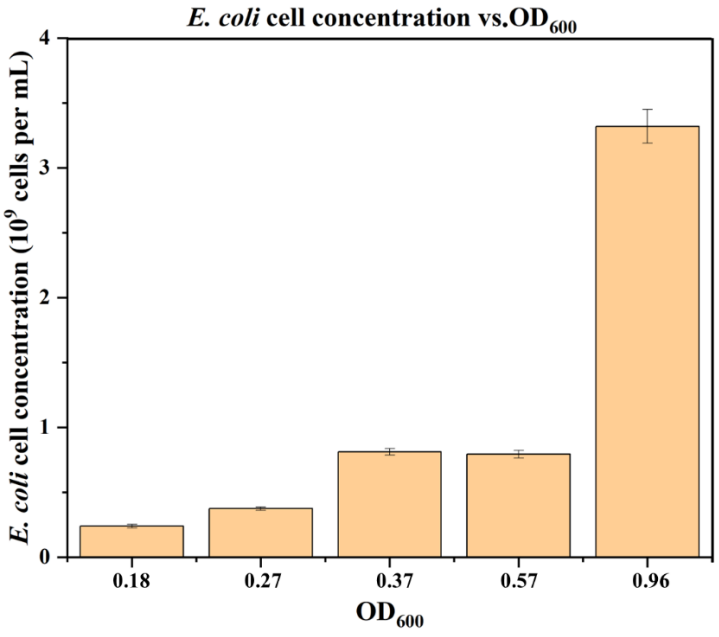

Figure S5: Bacterial concentration measured using FIJI for different OD_{600} measurements.

From **Table S7** and **Figure S5**, we clearly see that the standard deviation, standard error, and percent error are very low in comparison to the average values of the concentrations. The R^2 value was 0.86. This indicates that the image-processing technique gives precise measurements of the bacterial densities (see comparison of both methods in Figure S6).

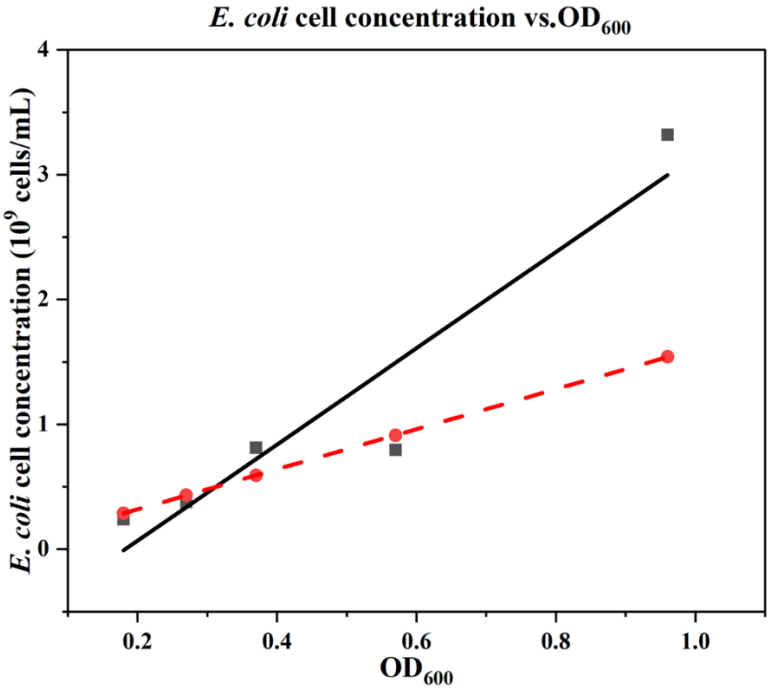

Figure S6: This figure represents the bacterial concentrations estimated using the image processing technique FIJI (squares) in comparison to the bacterial concentrations estimated by the OD_{600} method (these values are obtained by multiplying OD_{600} by 1.6 x 10^9 cells/mL) (circles).

Here, we notice that at lower bacterial concentrations, both methods give comparable estimations of the bacterial densities. However, these estimations diverge at higher concentrations.

References

1. Xu, T. et al. ProLuCID: An improved SEQUEST-like algorithm with enhanced sensitivity and specificity. J Proteomics 129, 16–24 (2015).

2. Tabb, D. L., McDonald, W. H. & Yates, J. R. DTASelect and contrast: Tools for assembling and comparing protein identifications from shotgun proteomics. J Proteome Res 1, 21–26 (2002).

3. Cociorva, D., Tabb, D. L. & Yates, J. R. Validation of Tandem Mass Spectrometry Database Search Results Using DTASelect. Curr Protoc Bioinformatics 16, 13.4.1-13.4.14 (2006).

4. Park, S. K., Venable, J. D., Xu, T. & Yates, J. R. A quantitative analysis software tool for mass spectrometry–based proteomics. Nature Methods 2008 5:4 5, 319–322 (2008).

5. Park, S. K. R. et al. Census 2: isobaric labeling data analysis. Bioinformatics 30, 2208–2209 (2014).

6. Peng, J., Elias, J. E., Thoreen, C. C., Licklider, L. J. & Gygi, S. P. Evaluation of multidimensional chromatography coupled with tandem mass spectrometry (LC/LC-MS/MS) for large-scale protein analysis: The yeast proteome. J Proteome Res 2, 43–50 (2003).

7. https://www.manula.com/manuals/ip2/ip2/1/en/topic/14-1-for-your-publications.